JGR Solid Earth

RESEARCH ARTICLE
10.1029/2019JB018052

Transient High Strain Rate During Localized Viscous Creep in the Dry Lower Continental Crust (Lofoten, Norway)

L. R. Campbell[1] and L. Menegon[1,2]

[1]School of Geography, Earth and Environmental Sciences, Plymouth University, Plymouth, UK, [2]The Njord Centre, Department of Geosciences, University of Oslo, Oslo, Norway

Key Points:
- Viscous creep at high differential stress and strain rate is observed in microstructures within lower crustal mylonitized pseudotachylytes
- The high stress and strain rate deformation was transient and localized, as shown by partial development of lower stress microstructures
- Pseudotachylytes could support transients in stress and strain rate within strong lower crust, for example, as observed during postseismic relaxation

Supporting Information:
- Supporting Information S1

Correspondence to:
L. R. Campbell,
lucy.campbell@plymouth.ac.uk

Citation:
Campbell, L. R., & Menegon, L. (2019). Transient high strain rate during localized viscous creep in the dry lower continental crust (Lofoten, Norway). *Journal of Geophysical Research: Solid Earth*, *124*, 10,240–10,260. https://doi.org/10.1029/2019JB018052

Received 17 MAY 2019
Accepted 27 SEP 2019
Accepted article online 14 OCT 2019
Published online 29 OCT 2019

Abstract Understanding the ability of the lower crust to support transient changes in stresses and strain rates during the earthquake cycle requires a detailed investigation of the deformation mechanisms and rheology of deep crustal fault rocks. Here, we show that lower crustal pseudotachylyte-bearing shear zones are able to accommodate short-term episodes of high strain rate and high stress deformation by accelerated viscous creep, followed by a reduction in stresses to some ambient deformation condition. Quartz microstructure within pseudotachylyte-bearing shear zones in otherwise undeformed granulites from Lofoten, Norway, indicates that dynamic recrystallization occurred during viscous creep under rapid strain rates and high stresses of ~10^{-9} s^{-1} and ~100 MPa, respectively. Lower stress microstructures (i.e., foam textures) are also recorded in the shear zones, indicating spatial and temporal variations of stress and strain rate during deformation cycles. Both the high and lower stress quartz recrystallization took place under granulite facies conditions of 650°C–750°C and 0.7–0.8 GPa and represented a record of highly localized viscous creep within the lower crust. This implies that lower crustal pseudotachylytes are potentially able to form extremely localized weak zones within strong lower crust, enabling a deep mechanical response to perturbations in stress and strain rate such as those experienced during the seismic cycle, for example, seismogenic loading followed by subsequent postseismic relaxation.

Plain Language Summary Detailed investigation of the strength and deformation style of fault rocks sourced from the Earth's lower crust is important to understand how the lower crust reacts to short-term variations in stress and strain rate, which can occur, for example, between earthquakes. Here, we show that solidified pseudotachylytes (initially melts produced due to frictional heating along the fault plane during an earthquake) occurring at depths of 25–30 km in the lower crust can accommodate deformation at particularly high strain rates and high stresses via solid-state creep. We look at pseudotachylytes formed in lower crustal shear zones that are now exhumed in Lofoten, Norway. Deformation microstructures in quartz within these pseudotachylytes have recorded rapid strain rates and high stresses. These microstructures are occasionally transformed into lower stress versions, indicating that during the deformation the stress and strain rate varied through both time and space. Both stages, however, record the same deformation temperatures and pressures, indicating that these are snapshots of ongoing deformation within the lower crust. We conclude that, when the lower crust is strong, pseudotachylytes will form important weak zones that accommodate deformation even during rapid variations in the deformation conditions, for example, as occurs during the postseismic period immediately after an earthquake.

1. Introduction

The rheological behavior of dry lower crustal rocks is commonly characterized by a cyclic interplay between viscous creep (mylonitization) and brittle, frequently coseismic, fracturing associated with formation of pseudotachylytes (Austrheim, 2013; Hawemann et al., 2018; Jamtveit et al., 2018; Menegon et al., 2017; Okudaira et al., 2015; Sibson, 1980; Wex et al., 2019; White, 1996). Earthquakes are effective precursors of ductile shear zones in dry and strong lower crustal regions, as they trigger rheological weakening by grain size reduction via fracturing and comminution alongside potential fluid infiltration (Jamtveit et al., 2019; Petley-Ragan et al., 2019). These processes may facilitate mylonitic creep, dominantly by grain size sensitive deformation localized to the hydrated volume of fractured rocks, commonly consisting of pseudotachylyte veins and their damage zone (Jamtveit et al., 2019; Menegon et al., 2017; Passchier, 1982; White, 1996).

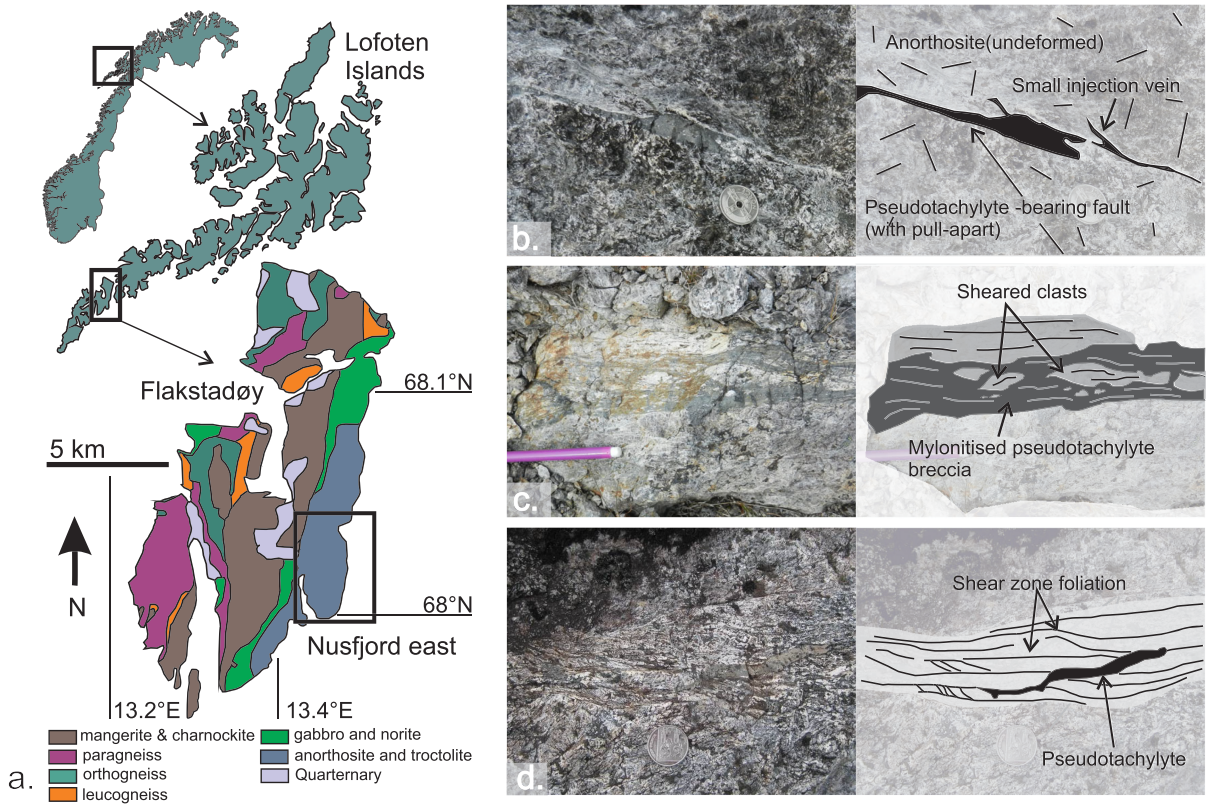

Figure 1. Pseudotachylytes in the Nusfjord region: (a) Geological map of Flakstadøy showing location of Nusfjord anorthosite ridge (after Steltenpohl et al., 2011); (b) typical non-mylonitized pseudotachylyte vein with pull-apart jog in anorthosite. Whitish border to vein margin is symptomatic of microcracking (coin diameter 2 cm); (c) sheared pseudotachylyte breccia forming part of localized shear zone; and (d) pseudotachylyte vein cross-cutting mylonite foliation within shear zone.

However, mylonitized pseudotachylytes may be overprinted by new generations of pseudotachylytes, thus indicating a cyclical interplay between aseismic creep and coseismic slip along the same structure (Menegon et al., 2017; Wex et al., 2019). This cyclical interplay already implies remarkable oscillations in stress and strain rate during the activity of lower crustal faults and shear zones presumably steered by the earthquake cycle. While this level of cyclical interplay is demonstrated in a number of detailed studies of exhumed lower crustal shear zones (Wex et al., 2019 and references therein), one existing question to address is whether the microstructures of lower crustal fault rocks can preserve a record of the rheological response to transient phenomena away from steady state creep rates. Investigating the microstructure of lower crustal fault rocks resulting from cyclical perturbations in viscous deformation conditions is particularly timely in the light of recent deformation experiments that demonstrate the ability of the recrystallized grain size of quartz to capture transients (Kidder et al., 2016).

Transiently elevated strain rates and stresses are observed in creeping faults from both the geological record (e.g., in the form of mutually overprinting pseudotachylytes and mylonites) and, at a more detailed temporal scale, from continuous geodetic observation of crustal deformation. In many cases, geodetic observations of elevated strain rates are ambiguous as to the contributing mechanisms and could be explained through the inclusion of frictional afterslip in addition to (or instead of) accelerated viscous creep in the mid-crust to lower crust (Fagereng & Biggs, 2019; Ingleby & Wright, 2017). It is clearly important, therefore, to understand the controls on where transient changes to crustal deformation rate are feasible, but the deformation mechanisms and materials and that can support rapid strain rates, and their subsequent decay are still debated. Important questions are, for example, whether transiently high postseismic strain rates require the presence of a weak material distributed under the seismogenic fault (Ivins, 1996) or if they can alternatively be accommodated within a single lithology with the appropriate rheology

(Chopra, 1997) and whether that rheology needs to be linear viscous (Thatcher, 1983), Burgers body (Hearn et al., 2002; Hearn et al., 2009), or power law (Ingleby & Wright, 2017). Therefore, understanding the geological record of transient rheologies in exhumed deep crustal fault rocks promises to be highly useful for constraining fault zone models used to explain surface deformation observations (Bürgmann & Dresen, 2008; Floyd et al., 2016).

In this contribution, we utilize an exhumed lower crustal shear zone network from the eastern Nusfjord region (Lofoten, Norway) to investigate processes that may facilitate rapid strain rates over short time scales within longer-term periods of steady state creep. Additionally, we consider the mechanisms of producing and maintaining localization of viscous deformation within dry, feldspar-rich lower crustal rocks, representative of intracontinental lower crustal shear zones in metastable, impermeable, and mechanically strong granulites (c.f., Austrheim et al., 1996; Jamtveit et al., 2018). We look at the deformation of pseudotachylytes that are initially produced by coseismic frictional melting but, once present, provide grain size and lithological contrasts that are susceptible to mylonitic overprinting. The Nusfjord pseudotachylytes have already been well constrained in terms of their mineralogy, water content, and pressure and temperature (P-T) conditions of mylonitic overprinting by Menegon et al. (2017), who concentrated on the deformation mechanisms that allow localization of viscous creep within pseudotachylyte in the lower crust. This current study utilizes these existing constraints but focuses on microstructural evidence for additional transient nonsteady-state episodes of viscous deformation that appear to have occurred locally and episodically within the ongoing mylonitization characterized by Menegon et al. (2017). We constrain the flow stress, strain rate, and viscosity of these transient perturbations and discuss the ability of pseudotachylyte to accommodate short-term variability in the conditions of solid-state viscous creep. We attempt to relate deformation conditions recorded by microstructures in exhumed fault rocks to creep rates and viscosities inferred from geodetic measurements during the postseismic and interseismic stages of the seismic cycle, thus bridging the gap between the geological record and the direct observation of earthquake cycle deformation.

2. Geological Setting and Sample Description

The Lofoten Islands in northern Norway (Figure 1a) are predominantly composed of Archaean to Paleoproterozoic ortho- and para-gneisses, intruded at 1.9–1.7 Ga by a suite of Anorthosite-Mangerite-Charnockite-Granite bodies (Corfu, 2004). These intrusions are anhydrous and emplaced under granulite facies conditions, which were estimated at 750°C–800°C and 0.4–1.2 GPa (Markl et al., 1998). The primary igneous textures and the dry granulite facies mineral assemblages are generally well preserved. Lofoten represents a tectonic window of basement rocks from the Baltica plate that are usually buried beneath the Caledonian nappe pile. The Lofoten basement rocks have largely escaped the Caledonian tectonometamorphic overprint as the result of the limited availability of fluids necessary to facilitate viscous deformation of the anhydrous, strong granulites (Steltenpohl et al., 2004).

Granulite, eclogite, and amphibolite facies localized shear zones are common in Lofoten and are frequently associated with large volumes of pseudotachylytes (Figure 1b). Available evidence indicates that these pseudotachylytes developed under lower crustal conditions and provided the necessary weak precursors on which mylonitic shear zones subsequently localized (Menegon et al., 2017). The Nusfjord anorthosite (Figure 1a) is cut by a network of localized shear zones that contain both pristine (Figure 1b) and mylonitized (Figures 1c and 1d) pseudotachylytes. Between these shear zones, the anorthosite is undeformed, preserving a coarse-grained igneous texture with up to 1- to 5-cm large crystals of plagioclase, associated with minor amounts (<10 vol.%) of clinopyroxene ± amphibole ± quartz ± orthopyroxene ± garnet ± biotite. Nonmylonitized, pristine pseudotachylytes (Figure 1b) range in thickness from <1 cm to ca. 10 cm and can be followed along strike for up to 100 m. Mylonitized pseudotachylytes are recognized in the field by the local preservation of pseudotachylyte breccia pockets and injection veins both along and across the mylonitic foliation (Figures 1c and 1d). They form shear zones that typically range in thickness from <1 cm to ~30 cm and that are continuous along strike for over 1 km on the eastern Nusfjord ridge. The thickest shear zones may have derived from the cyclical mylonitic overprint of several generations of pseudotachylytes, as indicated, at least locally, by the occurrence of pseudotachylyte veins discordant to the main mylonitic foliation and only partially transposed into it (Figure 1d). The shear zones also incorporate parts of the damage zone

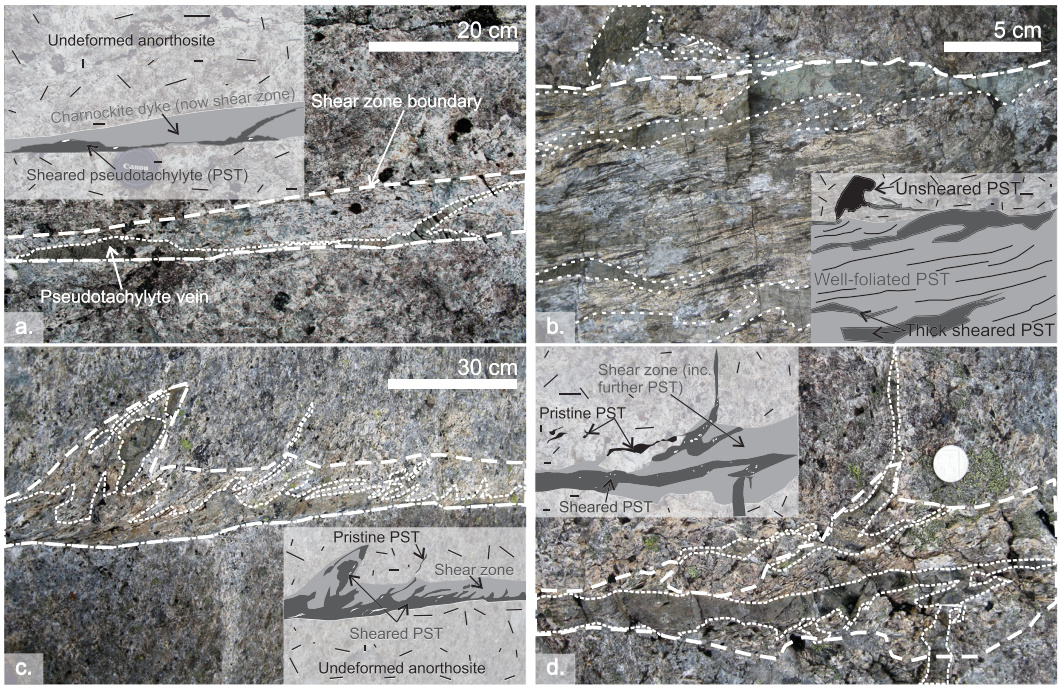

Figure 2. Typical field observations of shear zones (boundaries outlined with long dashed white lines) in Nusfjord anorthosite incorporating mylonitized pseudotachylytes ("PST," outlined in short dashed white lines): (a) sheared pseudotachylyte vein with flattened injection. Pseudotachylyte has exploited margins of a charnockite dike, which delineates the shear zone boundaries, site of samples 269C and 269E2 (68.0562°N 13.3646°E); (b) foliated mylonite consisting of multiple strands of sheared pseudotachylytes, including some thicker patches which appear to cut the foliation (68.0516°N 13.3694°E); (c) shear zone with significant amounts of mylonitized pseudotachylyte, with drag foliation developed along one side. A pristine pseudotachylyte is preserved some 10s of centimeters outside the shear zone. The sheared pseudotachylyte shows similar quartz microstructures to analyzed samples (see Figure S2a; 68.0557°N 13.3746°E); and (d) close-up along strike from 2c showing mylonitic shear of thick pseudotachylyte vein via the development of a strong oblique foliation. In turn, the thick vein cuts a foliated region apparently consisting of further sheared pseudotachylyte. Veins perpendicular to the shear zone trend become progressively less sheared with distance (top) or are unsheared (lower vein).

around pseudotachylyte veins, or alternatively anorthosite, charnockite, and granite dikes along which pseudotachylyte veins have exploited the boundaries (Figure 2a). This results in shear zones that are somewhat wider than any pseudotachylyte veins they incorporate (Figure 2) but nevertheless are of limited width restricted by the precursor structure. Mylonitized and nonmylonitized pseudotachylytes are observed adjacent to each other (Figures 2b–2d) in structural contexts where faults decorated with nonmylonitized pseudotachylyte cut undeformed anorthosite blocks between closely spaced (<20 m) mylonitized pseudotachylyte-bearing shear zones. These nonmylonitized pseudotachylyte faults appear to represent frictional deformation of the strong anorthosite host rock related to ongoing viscous creep on the shear zones and do not form in the same orientation as the shear zones (Figures 2c and 2d). Detailed field descriptions of the pseudotachylytes and shear zones can be found in Menegon et al. (2017).

The shear zone network in the Nusfjord east region consists of three main sets of shear zones, all containing variable amounts of mylonitized pseudotachylytes, although mylonitized pseudotachylytes are most extensively developed in the "set 1" shear zone orientation, dipping steeply toward the SE with normal-oblique kinematics (Figure 2b, Menegon et al., 2017). Mutual crosscutting relationships indicate that these three shear zone sets were broadly coeval. P-T conditions of pseudotachylyte formation and mylonitization were estimated at 650°C–750°C and 0.7–0.8 GPa, corresponding to an approximate depth range of 24–30 km (Menegon et al., 2017). ^{40}Ar-^{39}Ar dating of amphibole from localized amphibolite facies shear zones in the Nusfjord area with similar orientation to the Nusfjord east network yielded an age range of 433–413 Ma (Fournier et al., 2014; Steltenpohl et al., 2003). Given the similarity of structures, mineral assemblages and metamorphic conditions, this age range is also taken as representative of the Nusfjord east shear zone

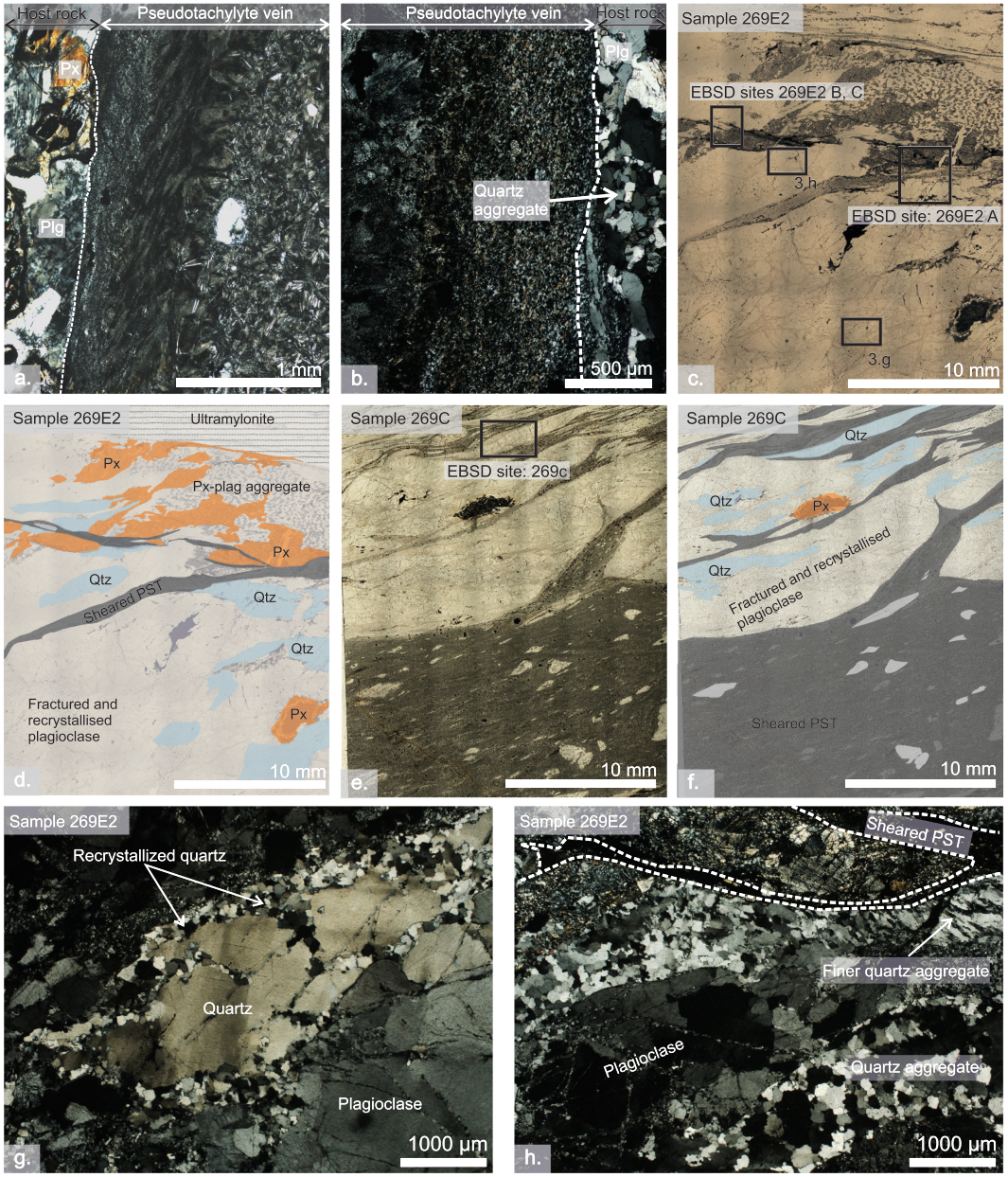

Figure 3. Microstructure of pseudotachylyte, mylonitized pseudotachylyte and quartz aggregates: (a) optical micrograph of the matrix of a non-mylonitized pseudotachylyte (cross-polarized light) with radiating feldspar microlaths grading into a fine-grained margin (68.0563°N 13.3775°E); (b) optical micrograph of the matrix of a non-mylonitized pseudotachylyte (cross-polarized light) with quartz in the immediate host rock margin (68.0557°N 13.3744°E); (c) optical micrograph (plane-polarized light) of thin-sheared pseudotachylyte veins in sample 269E2; (d) overlay on micrograph in 3c showing distribution of quartz, clinopyroxene, and sheared pseudotachylyte ("PST") within surrounding fractured plagioclase and ultramylonite band; (e) optical micrograph (plane polarized light) of sheared pseudotachylyte breccia (similar to the structure shown in 1c.) with flattened clasts and injection veins in sample 269c; (f) overlay on micrograph in 3e showing distribution of quartz, clinopyroxene, and sheared PST veins within surrounding fractured plagioclase forming the wider shear zone; (g) large quartz grain away from pseudotachylyte veins showing undulose extinction and mantle of recrystallized grains, sample 269E2; see c for location; and (h) variation in quartz microstructure with distance from (but also along strike of) a mylonitized pseudotachylyte vein. Location in sample 269E2 shown in part 3c.

network described here. The regional tectonic context at this time suggests that the Nusfjord shear zones represent the rheological response of the Baltica basement underthrusting Laurentia during the collisional (Scandian) stage of the Caledonian Orogeny.

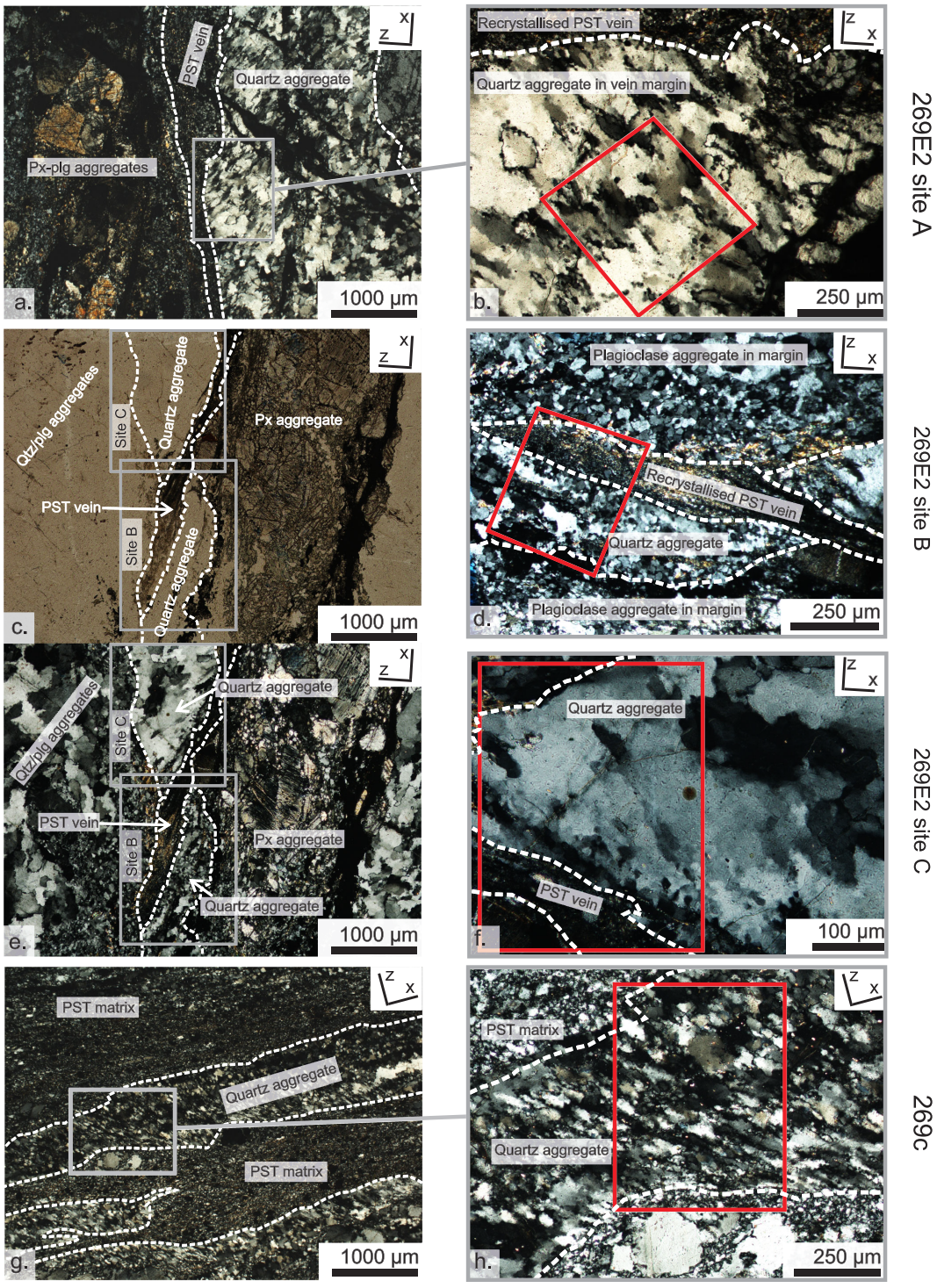

Figure 4. Microstructures of quartz around sites used for electron backscatter diffraction (EBSD) analysis. Grey boxes indicate location of higher magnification micrographs, red boxes indicate EBSD analysis sites, all cross-polarized optical micrographs except 4c, which is plane polarized. (a) sample 269E2 showing location of site A quartz aggregate in margin of sheared pseudotachylyte (PST) vein. Other phases in the host rock include plagioclase (Plg) and pyroxene (Px); (b) 269E2 site A at higher magnification. Note the serrated grain boundary indicative of bulging. (c) sample 269E2 in plane-polarized light showing quartz aggregates in sites B and C on opposite margins of a thin-sheared pseudotachylyte vein; (d) sample 269E2 site B at higher magnification; (e) cross-polarized version of part 3c; (f) sample 269E2 site C at higher magnification; (g) sample 269c, showing quartz ribbon surrounded by fine-grained pseudotachylyte matrix; and (h) sample 269C at higher magnification.

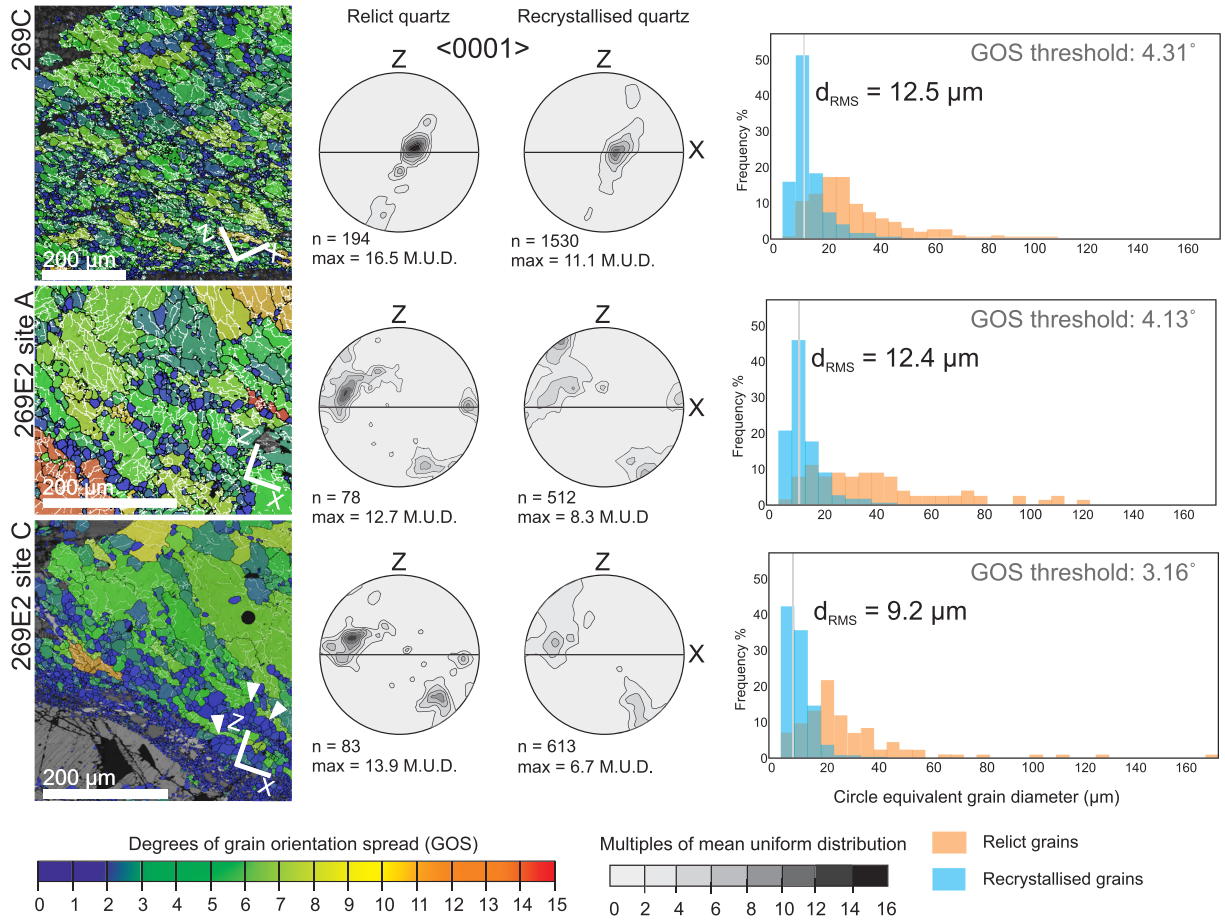

Figure 5. Grain orientation spread (GOS) maps of electron backscatter diffraction analysis sites in recrystallized quartz. The sense of shear is dextral. White arrowheads on site C map indicates contact of some foam texture quartz with the fine-grained recrystallized quartz. Pole figures (lower hemisphere) are shown for <0001> axes of relict and recrystallized quartz, with contouring at intervals of 2 multiples of uniform distribution (M.U.D) constructed with a half width of 10° and data clustering of 5°. Pole figures have been rotated into a standard reference frame (<*a*> axis pole figures are provided as Figure S4). Grain size distributions are shown for the analyzed populations of recrystallized (blue curve) and relict (orange curve) quartz grains distinguished by the stated GOS threshold.

Much of the primary structure of the mylonitized pseudotachylytes has been overprinted so that it is difficult to constrain any information about the nature of the seismicity that produced them. In addition, any brittle fault system that could potentially have extended these shear zones to structurally higher crustal levels is not preserved in the field around the Nusfjord area.

Pristine pseudotachylytes preserve a crystalline matrix consisting of plagioclase with some combination typically of amphibole, clinopyroxene, orthopyroxene, biotite, and K-feldspar. Pseudotachylyte veins may be enriched in biotite, K-feldspar, and quartz, either in the crystalline matrix or in unmelted clasts, where the pseudotachylytes cut through granitic and charnockitic pods or dikes. Mylonitized pseudotachylyte-bearing shear zones contain sheared clasts of dismembered and partially recrystallized plagioclase, sometimes in combination with partially transposed and flattened injection veins (Figure 3), and melt quenching-related microstructures such as spherulites, dendritic crystals, and microlites (e.g., Figures 3a and 3b) are not preserved. The amount of strain recorded in the mylonitized pseudotachylytes varies from low, as indicated by the moderate inclination of elongated survivor clasts with respect to the shear zone boundary (Figure 2d in Menegon et al., 2017), to very high, as indicated by the development of a strongly banded mylonitic foliation where clasts of host rock are flattened and elongated parallel to the shear zone boundary (Figure 2b). The deformation microstructures analyzed in this study have been observed in a large number of samples of pseudotachylyte-bearing shear zones from Nusfjord east. Here, we present the detailed microstructural analysis of representative samples from shear zone "269" (samples 269C and 269E2: Figures 3 and

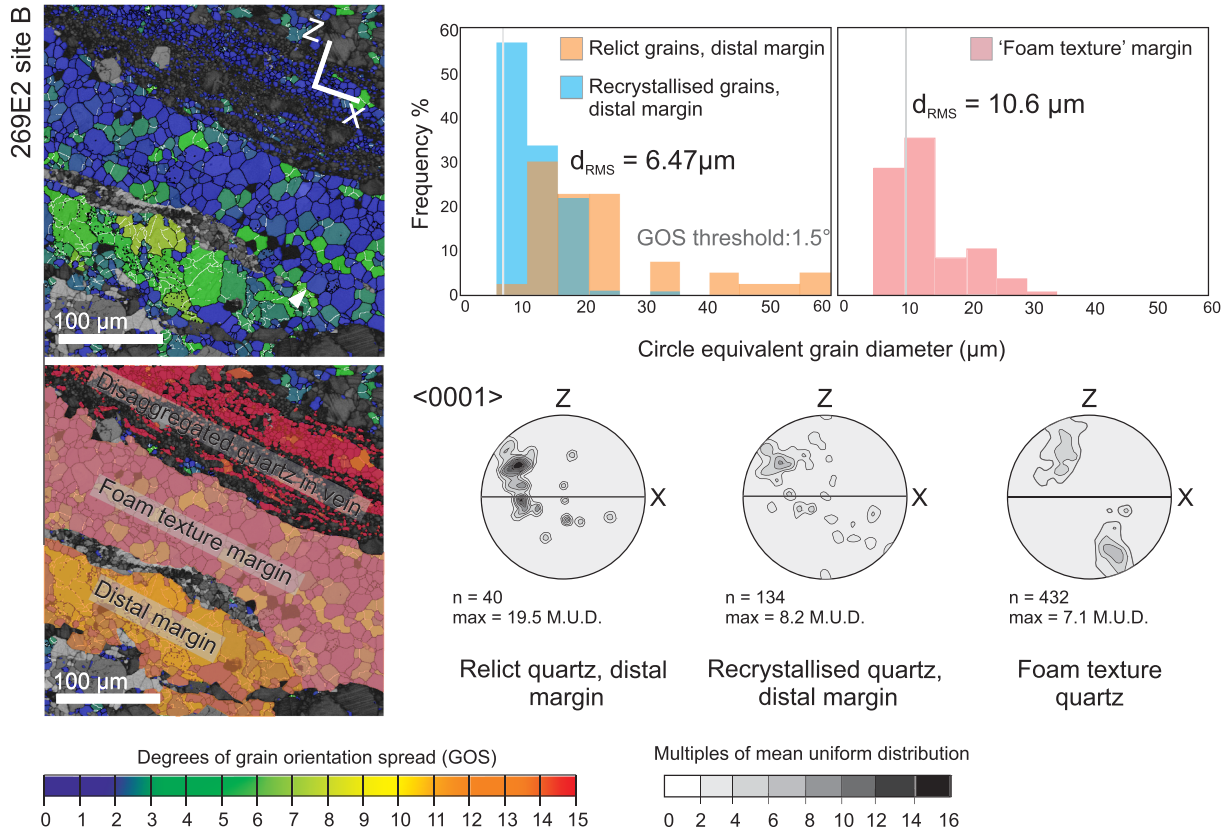

Figure 6. Grain orientation spread (GOS) map and electron backscatter diffraction analysis of recrystallized quartz in sample 269E2 site B. A second (lower) copy of the map includes colored overlays indicating the different quartz domains referred to in the text. This sample was not used for piezometry due to the development of "foam texture" in the immediate margin to the mylonitized pseudotachylyte. White arrowhead on upper map indicates contact of foam texture quartz with the more distal margin displaying some fine-grained recrystallized quartz. <0001> axes pole figures and grain size distributions are shown for the relict and recrystallized quartz in the distal margin and for the foam-textured quartz (<*a*> axis pole figures are provided as Figure S4). The sense of shear is dextral. Pole figures have been rotated into a standard reference frame.

4). The shear zone has the typical set 1 orientation and kinematics (dip-and-dip direction: 76/138) and includes a mylonitized pseudotachylyte vein exploiting the boundary of a charnockite dike (Figure 2a), which is also variably sheared along strike. The shear zone can be traced discontinuously for around 10 m, and the samples were located approximately the same distance along strike from each other.

3. Methods

3.1. EBSD

The electron backscatter diffraction (EBSD) data were acquired using a JEOL 7001 FEG-SEM equipped with a NordLysMax detector at the Electron Microscopy Centre of the University of Plymouth. Polished thin sections were carbon-coated prior to EBSD analysis. Working conditions during acquisition of the EBSD patterns were 20-kV accelerating voltage, 12-nA probe current, 70° sample tilt, ~20 mm working distance and high vacuum. EBSD patterns of quartz were acquired and indexed with the AZtec software (Oxford Instruments) on four rectangular grids from two samples of mylonitized pseudotachylytes, 269C and 269E2 (Figures 3c, 3e, and 4), with step sizes ranging from 0.4 to 1.2 μm and using the "quartz-new" match unit from the HKL-Oxford Instruments' database. EBSD data were processed using the Channel 5 software (Oxford Instruments).

EBSD data are presented as grain orientation spread (GOS) maps, as quartz *c*-axis pole figures, and as grain size distribution histograms. The GOS is a measure of the internal strain of a grain defined as the average misorientation angle between each pixel in a grain and that grain's mean orientation (Wright et al., 2011).

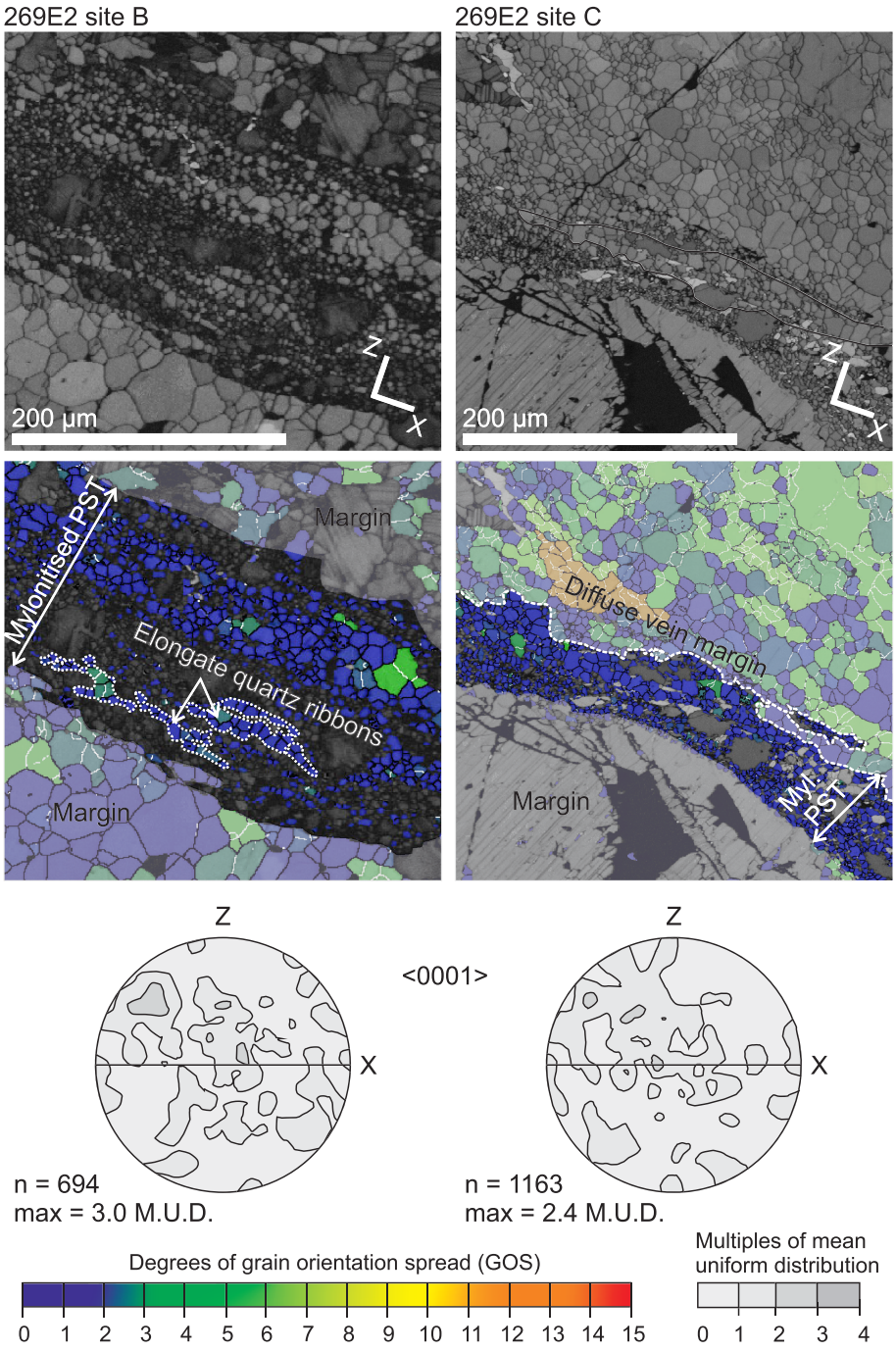

Figure 7. Details of disaggregated quartz in mylonitized pseudotachylyte ("myl. PST") veins. Upper images are band contrast images, center images are grain orientation spread (GOS) maps of quartz, bottom pole figures show <0001> axes plotted on lower hemisphere equal area projections (note change in contouring compared to Figures 5 and 6).

The orientation of quartz *c*-axis was plotted on contoured pole figures (lower hemisphere of the equal angle projection) as one point per grain. The pole figures are oriented in the plane containing the pole to the mylonitic foliation (the *Z*-axis) and the stretching lineation (*X*-axis). The orientation of the *X*-axis and *Z*-axis is shown on each GOS map. The grain size distribution histograms were plotted as frequency (in percent) versus grain size (in micrometer) calculated as the diameter of the circle with an area equivalent to that of the grain.

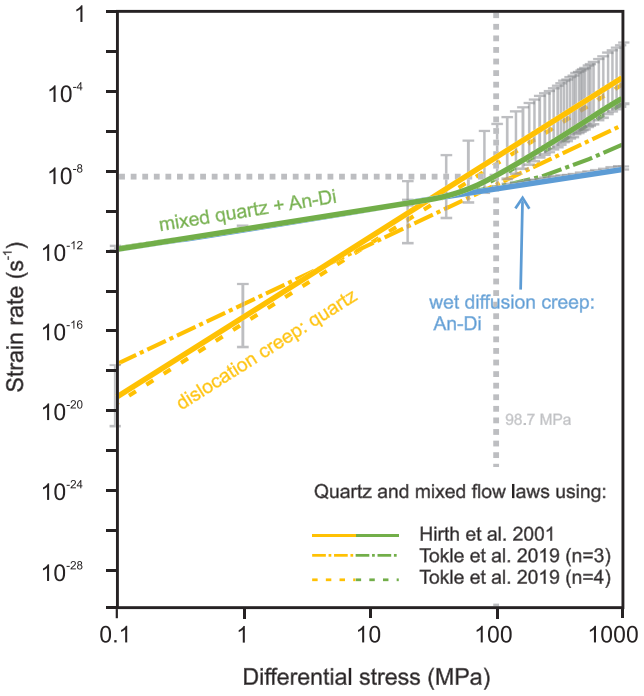

Figure 8. Flow laws calculated for mylonitized pseudotachylyte-bearing shear zones at 700°C (error bars show the uncertainty relating to the predicted temperature range of 650°C–750°C added to the empirical uncertainty of the experimental flow laws). Shown are dislocation creep of quartz (Hirth et al., 2001; Tokle et al., 2019), wet diffusion creep of the anorthite-diopside matrix (Dimanov & Dresen, 2005), and a composite flow law for 10% quartz and 90% anorthite-diopside matrix. Dashed grey line shows differential stress calculated from quartz piezometry and resultant strain rate from mixed flow law.

3.2. Flow Stress, Strain Rate, and Viscosity Calculations

The EBSD-calibrated recrystallized grain size piezometer for quartz of Cross et al. (2017) was used to calculate the flow stress of mylonitization. Recrystallized quartz grains were distinguished from the relict grains by their GOS. The critical GOS value corresponding to the threshold between relic grains and recrystallized grains was established from the "kneepoint" in the cumulative frequency plot of GOS for the entire quartz population (Figure S1). The root mean squared grain size (D_{RMS}) of the recrystallized quartz grains was used in the "sliding" piezometer of Cross et al. (2017), which states $D = 10^{4.22\pm0.51}\ \sigma^{-1.59\pm0.26}$, where D is the mean grain size and σ is the flow stress.

The dislocation creep flow laws for quartz of Hirth et al. (2001) and Tokle et al. (2019) were used to calculate and compare possible strain rates for quartz, based on the deformation microstructures characterized in section 4.1. For the recrystallized pseudotachylyte matrix, the wet diffusion creep flow law for an anorthite-diopside aggregate (Dimanov & Dresen, 2005) was chosen as appropriate due to the fine grain size and lack of crystal preferred orientation (CPO) in Nusfjord pseudotachylytes, as suggested by Menegon et al. (2017). In Nusfjord, the pseudotachylytes are relatively hydrated relative to the host rock and the H_2O content of the recrystallized pseudotachylyte is 0.2–0.4 wt.% (Menegon et al., 2017), above that of the "wet" samples (0.05 wt.%) of Dimanov and Dresen (2005), and hence, the wet flow law was chosen. The H_2O content of the experiments compiled in Tokle et al. (2019) sit in the range 0.1–0.4 wt.% and are therefore very similar to these Lofoten samples.

To represent deformation of the entire pseudotachylyte-bearing shear zone, a simple mixed flow law was calculated for 10% quartz deformed by dislocation creep and 90% anorthite-diopside deformed by diffusion creep, in the form $\dot{\varepsilon}_{\mathrm{mixed}} = \left[X_{\mathrm{quartz}}\dot{\varepsilon}_{\mathrm{quartz}} + X_{An-Di}\dot{\varepsilon}_{An-Di}\right]$ where $\dot{\varepsilon}_{\mathrm{mixed}}$ is the strain rate of the mixed flow law, X denotes the fraction and $\dot{\varepsilon}$ is the strain rate of quartz and anorthite-diopside, respectively. The strain rates were multiplied by $\sqrt{3}$ to convert from axial to shear strain rates (Paterson & Olgaard, 2000); 10% is perhaps an overestimate of quartz content in pseudotachylyte-bearing shear zones in Nusfjord east, but the mixed strain rate proves insensitive to small adjustments in quartz volume.

Effective viscosity of the pseudotachylyte-bearing shear zones was calculated from the flow stress and the strain rate (using the Hirth et al., 2001 flow law to model the contribution of dislocation creep of quartz) as $\eta = \sigma/2\dot{\varepsilon}$, where σ is the flow stress and $\dot{\varepsilon}$ the strain rate. Errors were propagated through the process from the uncertainties in temperature and pressure (as stated in Menegon et al., 2017) as well as the errors published for parameters in the flow laws and piezometric relations.

4. Results

4.1. Microstructure, Crystallographic Preferred Orientation, and Grain Size of Quartz in Pseudotachylyte-bearing Shear Zones

Monomineralic quartz domains are locally present within shear zones in different textural positions: (1) in deformed host rock domains at the immediate margins to mylonitized pseudotachylyte veins in mylonitized breccias (Figures 1c, 3c, 3d, and 4a–4f), (2) in ribbons entirely wrapped by the recrystallized pseudotachylyte matrix within mylonitized brecciated networks, (Figures 3e, 3f, 4g, and 4h), and (3) as thin (50–200 μm thick), elongate ribbons within sharp mylonitized veins derived from the pseudotachylyte generation surfaces (Figure S2a). In all these domains, quartz occurs as recrystallized fine grains mantling larger grains. The large grains show undulose extinction and shape elongation (Figures 4b, 4d, and S3) and contain a high density of low-angle boundaries that define subgrains of the same size of the recrystallized grains (Figure 5). The smaller grains have low GOS values (typically ≤4.3°; Figure 5), which are used to separate the

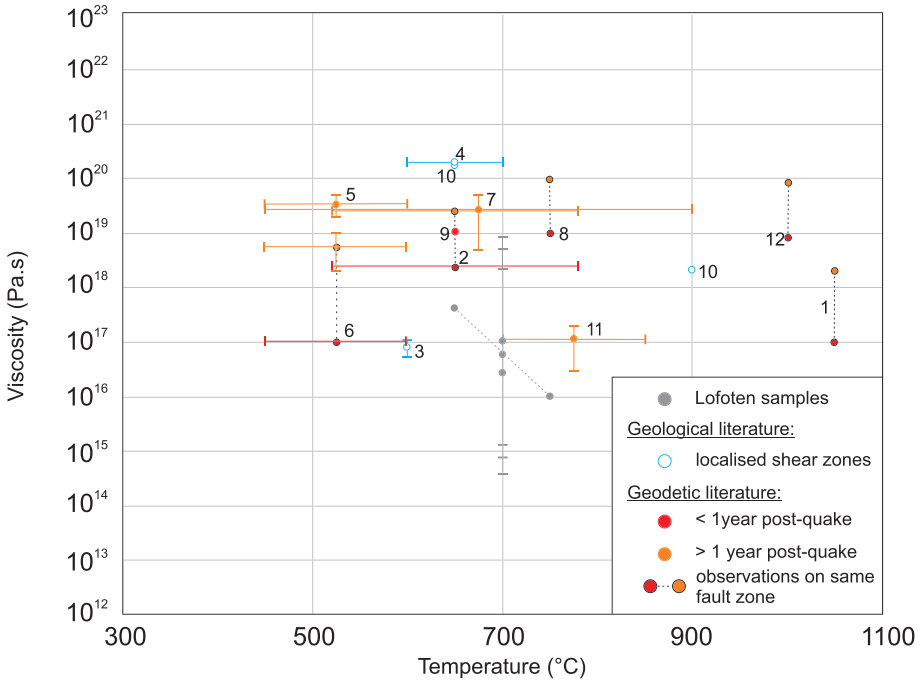

Figure 9. Effective viscosities of Nusfjord mylonitized pseudotachylytes, and comparable values taken from geological and postseismic geodetic studies. Datapoints are numbered as follows: 1, Freed et al. (2006); 2, Freed and Burgmann (2004); 3, Gardner et al. (2016); 4, Getsinger et al. (2013); 5, Hearn et al. (2009); 6, Hearn et al. (2002); (7) Hetland and Hager (2003); (8) Kenner and Segall (2003); 9, Pollitz et al. (2001); 10, van der Werf et al. (2017); 11, Vergnolle et al. (2003); 12, Zhao et al. (2017). Geodetic studies are classified by the timescale of observation.

populations of recrystallized grains from the larger relict grain population (Cross et al., 2017). Where quartz occurs further away (Figures 3g and 3h) from the sheared pseudotachylyte veins, it lacks both the shape elongation and the frequency of finer grains that is observed in the immediate vicinity to the veins. Quartz, plagioclase, and clinopyroxene in the proximal damage zone flanking pristine pseudotachylytes do not show evidence of crystal plastic deformation and dynamic recrystallization (Figures 3a and 3b).

The <*c*> axis pole figures for the recrystallized and relict quartz grains are very similar at each analyzed site (Figure 5). In sample 269C, <*c*> axis orientations form an incomplete single girdle with a maximum near the center of the pole figure. In sample 269E2, at analysis sites A and C, the <*c*> axes form maxima oblique to the mylonitic foliation (Figure 5).

In sample 269E2, site B (Figure 6) shows a region characterized by well-developed quartz triple junctions, equant grain shape, low GOS, and a larger grain size than the rest of the recrystallized population, similar to foam textures described in Kidder et al. (2016). These grains have a similar CPO to the relict and finer recrystallized quartz aggregates preserved locally elsewhere around the margin of this vein (Figures 5 and 6). Similar features are seen very locally within site C (Figure 5).

Within mylonitized pseudotachylyte veins, quartz locally occurs also as dispersed grains within the vein matrix (Figures 5–7). This appears to be the result of the progressive disaggregation of polycrystalline recrystallized ribbons leading to phase mixing (Cross & Skemer, 2017; Kilian et al., 2011). One-grain-wide elongate ribbons parallel to the vein margins are progresisvely detached from the margin quartz aggregates (Figure 7), and individual quartz grains are separated from the main ribbon by grains of other phases (mostly plagioclase). The crystallographic preferred orientation of the disseminated quartz grains is very weak or absent (Figure 7). The foam-textured regions, the disseminated quartz in the vein, and the thinnest recrystallized ribbons (only 1–2 grains in width) were excluded from grain size calculations used for piezometry due to the effects of annealing and second-phase pinning on the grain size (Herwegh et al., 2011).

In summary, we interpret the quartz microstructure as indicative of dislocation creep and dynamic recrystallization by dominant subgrain rotation, based on the occurrence of core-and-mantle microstructures, on the

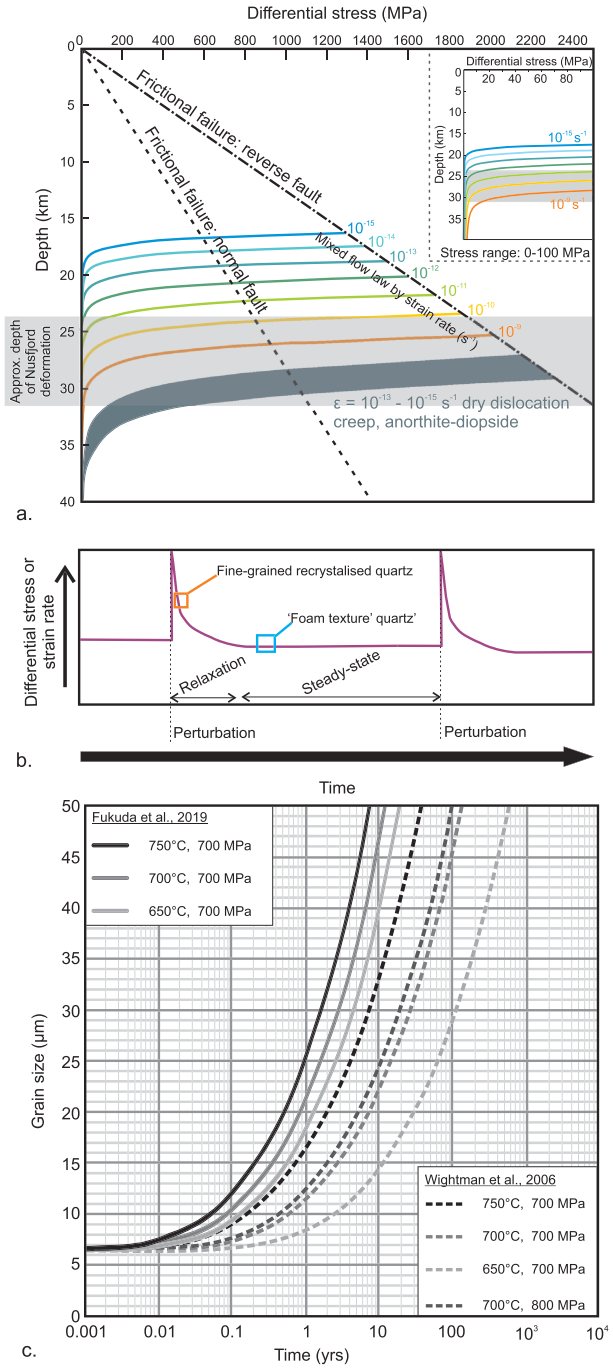

Figure 10. Crustal strengths and strain rates recorded in the Nusfjord mylonitized pseudotachylytes: (a) crustal strength diagram with likely depth of Nusfjord east shear zones indicated in grey box. A Poisson's ratio of 0.233 (Ji et al., 2014), a frictional coefficient of 0.75 (Sibson, 1974), a density of 2,700 kg/m^3, and a theta of 60°are used to calculate the frictional failure law following the method of Sibson (1974). A geothermal gradient of 25°C/km is assumed. The calculated mixed flow law combining dislocation creep of quartz and diffusion creep of an anorthite-diopside aggregate is shown for the transient fast strain rate (10^{-9} s^{-1}, orange curve) and a "typical" (Fagereng & Biggs, 2019) steady state strain rate (10^{-15} s^{-1}, blue curve) as well as the intermediate strain rates that would be experienced during relaxation. Also shown is the dry dislocation creep flow law for an anorthite-diopside aggregate (grey curve; Dimanov & Dresen, 2005) to represent the hypothetical viscous deformation of the bulk anorthosite. The inset magnifies the mixed flow laws at low flow stress; (b) microstructures observed in quartz in mylonitized pseudotachylytes in Nusfjord related to relaxation of stress and strain rates over time after some perturbation, for example, seismic slip; and (c) static grain growth of quartz from an initial grain size of 6.5 μm modeled for Nusfjord deformation temperatures and pressures using the quartz grain growth parameters of Wightman et al. (2006) and Fukuda et al. (2019).

similar size of subgrains and of recrystallized grains, and on the overlap in the *c*-axis crystallographic preferred orientation between relict grains and recrystallized grains (Figure 5). The similarity between subgrain size and recrystallized grain size indicates that grain growth after subgrain rotation recrystallization was negligible. On the other hand, the local development of foam texture quartz is likely to be the result of static annealing.

The root-mean-squared grain sizes of the recrystallized quartz populations are 12.5, 12.4, and 9.2 μm for samples 269C, 269E2 site A, and 269E2 site C, respectively. Using the sliding piezometer calibrated by Cross et al. (2017), these recrystallized quartz populations suggest flow stresses of 92.0, 92.3, and 111.7 MPa, giving a mean flow stress across these samples of 98 ± 18 MPa (2σ).

4.2. Estimate of Strain Rates in Pseudotachylyte-bearing Shear Zones

The rheology of quartz-bearing pseudotachylyte shear zones in Nusfjord east was modeled using a mixed flow law that considers a 10% volume fraction of quartz deforming by dislocation creep (flow laws from Hirth et al., 2001 and Tokle et al., 2019) and a 90% volume fraction of anorthite-diopside aggregate deforming by wet diffusion creep (flow law from Dimanov & Dresen, 2005), based on the typical proportions of quartz in and around the mylonitized pseudotachylytes (see section 3.2).

At temperatures of 700°C and flow stress of 98 MPa, the predicted strain rates for all flow laws fall within the range of 10^{-10}–10^{-7} s^{-1} (Figure 8). At this bulk flow stress, wet dislocation creep of quartz allows deformation at a faster strain rate than wet diffusion creep of anorthite-diopside. Mylonitization of the pseudotachylyte involved concurrent dislocation creep of the quartz ribbons and grain size sensitive creep of the anorthite-diopside matrix, similar to other deformed and recrystallized pseudotachylytes (Price et al., 2012; White, 1996). We use the flow stress derived from quartz piezometry to calculate all strain rates, including in the mixed flow law that combines the behavior of quartz and the pseudotachylyte matrix (the evidence behind this assumption of constant stress is discussed in section 5.1). At a flow stress of 98 MPa, the mixed flow law using the Hirth et al. (2001) quartz dislocation creep flow law results in a strain rate of 6.3×10^{-9} s^{-1}. Quartz dislocation creep flow laws are also shown from Tokle et al. (2019), with stress exponents of $n = 3$ and $n = 4$; using these to represent quartz in a mixed flow law at a stress of 98 MPa results in strain rates of 1.4×10^{-9} and 3.4×10^{-9} s^{-1}, respectively. Since these resultant mixed flow law strain rates are very similar, only the mixed flow law using the Hirth et al. (2001) quartz dislocation creep flow law is used in subsequent calculations of viscosity. The choice of these flow laws is discussed in section 5.1. The mixed flow laws, being combined from both diffusion creep (linear viscous) and dislocation creep (power law) flow laws, are inherently non-linear.

4.3. Estimate of the Effective Viscosity of Mylonitized Pseudotachylyte

The effective viscosity of the Nusfjord mylonitized pseudotachylytes deforming at 700°C is 3.6×10^{16} Pa·s using the strain rate of 6.3×10^{-9} s^{-1} derived from the mixed quartz + anorthite-diopside flow law and the flow stress of 98 MPa. When compared to equivalent temperature estimates from geodetic and geological studies of the viscosity of the lower crust (Figure 9), this result is comparable with the lowest values reported, although most literature values are at least an order of magnitude higher. The lack of viscous deformation observed in the anorthosite outside the shear zones suggests that much higher stresses than ever were present would be needed to induce viscous creep in the anorthosite. Hence, it would be unrealistic to combine an anorthosite viscosity with the mylonitized pseudotachylyte viscosity to represent the entire ~1-km crustal width encompassed by the shear zone network. Additionally, the anorthosite viscosity under dry dislocation creep (Dimanov & Dresen, 2005) would be several orders of magnitude higher than reported literature values, being around 10^{24} Pa·s (Figure 9). In order to ensure that they represent deformation of fault zones at depth, all geodetic values shown in Figure 9 are derived from postseismic observations. The geological studies do not necessarily identify any association with seismogenic indicators but are taken from observations of shear zones and hence are inherently localized.

5. Discussion

5.1. High Strain Rate Transients Preserved in the Quartz-recrystallized Grain Size

Recrystallized quartz in the mylonitized pseudotachylytes (Figures 4, 5, S2, and S3) presents microstructures typical of bulging and subgrain rotation recrystallization. These microstructures are more generally

associated with deformation temperatures up to 500°C (e.g., Stipp et al., 2002) rather than the 700°C ± 50°C established for the viscous deformation of the Nusfjord east pseudotachylyte (Menegon et al., 2017). However, there is no evidence that quartz recrystallization occurred during a lower temperature overprint, in that recrystallized quartz coexists with neoblasts of clinopyroxene (Figure S2b), pargasitic amphibole and calcic plagioclase in the mylonitic foliation (Menegon et al., 2017). Additionally, the *c*-axis orientations of the fine and coarse grains are the same (Figures 5 and 6), whereas if the recrystallized grains were redeformed by some later event, some differences in the CPO might be expected. Any undetected lower temperature viscous overprint of the pseudotachylytes seems unlikely, as the temperature estimate was derived from thermodynamic modeling of the whole pseudotachylyte vein assemblage and from amphibole-plagioclase geothermobarometry using amphibole grains that grew into synkinematic dilatant sites (Menegon et al., 2017). Fine-recrystallized grain size of quartz in lower crustal shear zones has been attributed to dry conditions during deformation that inhibit efficient recovery (Fitz Gerald et al., 2006; Menegon et al., 2011), which would be one explanation for the occurrence of "low-temperature" quartz microstructures at 700°C. However, the Nusfjord mylonitized pseudotachylytes deformed under locally H_2O-present conditions that facilitated the nucleation of amphibole along grain and phase boundaries (Menegon et al., 2017). Thus, we interpret the apparent low-temperature microstructure of the fine-grained recrystallized quartz to instead be the result of high stress and strain rate deformation at the same P-T conditions of 700°C and 0.8 GPa suggested by Menegon et al. (2017) for the long-term viscous creep in the mylonites. This reinforces that care should be taken when qualitatively attributing deformation temperatures to microstructures due to the accompanying trade-off between strain rate, water content, and stress (Hirth & Tullis, 1992; Piazolo et al., 2002; Tokle et al., 2019).

Two published flow laws are compared in Figure 8 for dislocation creep of quartz and the resultant mixed flow laws (Hirth et al., 2001; Tokle et al., 2019). Both have been chosen for their attempts to reconcile experimental with natural deformation conditions and inclusion of microstructural comparisons. The more recent work of Tokle et al. (2019) suggests that the stress exponent of quartz dislocation creep flow laws may change with changing deformation temperatures and stresses — at high stress and low temperatures, $n = 3$ is deemed most applicable, and at low stress and high temperatures, $n = 4$. Around the calculated differential stress of 98 MPa, all the quartz flow laws in fact give a mixed flow law strain rate on the order of 10^{-9} s^{-1} (Figure 8), so we are confident that this figure is not biased by the choice of published flow law. Under these deformation conditions, the Tokle et al. (2019) flow law using a stress exponent (n) of 4 predicts that prism <*a*> will be the rate-limiting slip system, whereas basal <*a*> is predicted to be the rate-limiting slip system for the $n = 3$ flow law. In the Nusfjord samples, 269C shows a CPO maxima near to the *Y*-axis (Figure 5), consistent with prism <*a*> slip. However, the CPOs for the analyzed sites in sample 269E2 are less clear but more suggestive of a mix of basal <*a*> and rhomb <*a*> slip. At 98 MPa flow stress, as calculated from the quartz piezometry, the $n = 4$ flow law is marginally faster (weaker) than the $n = 3$ flow law (Tokle et al., 2019), so the $n = 4$ slip on prism <*a*> would be expected to occur if the conditions made that feasible. Tokle et al. (2019) also state that the $n = 4$ flow law is applicable under low stress (and/or high temperature) conditions, and the $n = 3$ law under higher stress (and/or lower temperature). It is difficult to extrapolate the experimental temperatures and pressures to compare with our natural conditions, but we suggest that the difference in CPO between samples 269C and 269E2 do not represent a stress difference, based on the similar piezometry results, and so do not warrant the attribution of separate flow laws with different stress exponents. With reference to the choice of flow law to represent the pseudotachylyte matrix, although amphibole is also present, its CPO suggests that it deformed via diffusion creep (Menegon et al., 2017). Amphibole deforming by diffusion creep under lower crustal temperature and pressure conditions displays similar strength to wet anorthite deforming by diffusion creep (Getsinger & Hirth, 2014). Hence, we prefer to use the established anorthite-diopside flow laws (Dimanov & Dresen, 2005) rather than attempt to account for amphibole behavior.

Calculation of strain rates for the anorthite-diopside pseudotachylyte matrix, and of the combined flow law, assumes that the flow stress calculated from quartz piezometry is homogeneous across the vein. Although the deformation mechanisms in the recrystallized polymineralic pseudotachylyte matrix and in the monomineralic quartz aggregates were different (diffusion creep and grain boundary sliding in the recrystallized pseudotachylytes vs dislocation creep in quartz), there does not seem to be any microstructural evidence for a significant viscosity contrast between the quartz where it occurs in monomineralic ribbons within

the vein and the matrix of the pseudotachylyte (Figures 3e, 3f, 4a, 4e, and 4g), whereas pinch-and-swell, buckling, and boudinage microstructures might be expected if there were. These microstructures are expected to form even at small strains (Gardner et al., 2016). In the absence of clear evidence of viscosity contrasts between monomineralic recrystallized domains and polymineralic matrix, recrystallized grain size paleopiezometry has yielded representative results in the study of shear zone rheology elsewhere in the lower crust (e.g., Mehl & Hirth, 2008; Viegas et al., 2016; Wex et al., 2019), and here, we adopt the same approach. In addition, in the context of Voigt-Reuss elastic limits, this constant-stress state indicates the lower (Reuss) bound for the bulk viscous strength of the pseudotachylyte vein (Hill, 1965), but noting the similarity in strain rates for quartz and for anorthite-diopside aggregates at the predicted flow stress (Fig. 8), the upper Voigt bound (constant strain rate) is not expected to be significantly different. Hence, either both strain rate and stress were approximately constant across the vein, or both must vary in complementary ways to maintain the constant bulk viscosity.

We consider the quartz deformation outlined here as representative of the transient high stress deformation localized in the pseudotachylyte-bearing shear zones. This is supported by the observation that the systematic occurrence of fine-grained recrystallized populations is limited to the proximity to the mylonitized pseudotachylyte veins or to their interior (compare Figures 3g, 3h, and 4), arguing for highly localized enhanced strain rate in the mylonitized pseudotachylytes. In addition, the quartz deformation cannot predate the pseudotachylyte formation, because the quartz in the damage zone of unmylonitized pseudotachylytes is also undeformed (Figure 3b). Although quartz is present only in limited amount (ca. 10 vol.%) within and around the analyzed mylonitized pseudotachylyte veins, the low variation of recrystallized grain sizes and resultant flow stresses for samples from different shear zone strands suggests that discontinuous aggregates of quartz are able to consistently capture the high strain rate deformation localized to the sheared pseudotachylytes.

Support for the short-term transience of the high stress, high strain rate state is provided by local low stress overprinting of the fine-grained recrystallized quartz. In sample 269E2 site B (Figure 6), quartz at the immediate margin of the mylonitized pseudotachylyte forms a band of much coarser grains than the adjacent recrystallized quartz and has lower internal misorientation than the larger relict grains contained in the same region. Equant grains and 120° triple junctions are also common in this coarser quartz band (Figure 6). The quartz in this immediate margin region have a CPO with similar orientation of <*c*> axes to the relict and fine-recrystallized quartz populations of the more distal margin, forming maxima moderately oblique (in a clockwise direction) to the trace of the foliation with some dispersion extending out toward the *Y*-axis. This preservation of the CPO during annealing, combined with a slight weakening of the CPO, is consistent with the findings of quartz static annealing studies (Heilbronner & Tullis, 2002). A partial development of a similar microstructure is also observed in the margin to the pseudotachylyte vein in sample 269E2 site C (Figure 5), where some of the recrystallized grains with low GOS values are larger than the typical subgrain size in this sample and also display 120° triple junctions. These features are classified as a foam texture, which has been shown to develop in quartz as a response to a rapid decrease in stress (Kidder et al., 2016). The grains at the edges of the foam-textured domains appear to be growing over the domains of relict and fine-grained recrystallized quartz (Figures 5 and 6). We interpret this contrast between the finer-grained and the foam-textured recrystallized quartz populations to represent two stages of progressive deformation, as indicated by the consistent CPO. Partial overprinting of the fine-grained recrystallized population by the foam-textured quartz may represent a localized record of the stress decrease during the creep following the high stress transient (e.g., Trepmann et al., 2007). The high stresses and strain rates recorded from the finer recrystallized quartz are therefore a snapshot of temporary transient deformation conditions, in line with recent experimental results that demonstrated the ability of quartz microstructures and grain size to capture transients (Kidder et al., 2016). Our interpretation, therefore, is that in the Nusfjord mylonitized pseudotachylytes, the relict and fine-grained recrystallized quartz populations record an initial transient high stress and high strain rate deformation event localized within the sheared pseudotachylyte.

The flow stress of 98 MPa recorded in the recrystallized grain size of fine-grained quartz in mylonitized pseudotachylytes is higher than the differential stresses typically estimated for shear zones at lower crustal depths (Behr & Platt, 2014; Getsinger et al., 2013), but transient high stresses hundreds of megapascals higher than steady-state have been observed and modeled for natural shear zones near the frictional-viscous transition (Ellis & Stöckhert, 2004; Küster & Stöckhert, 1999; Matysiak & Trepmann, 2012; Trepmann & Stöckhert, 2003). This scenario fits with the likely depth range and nature of viscous deformation on the Nusfjord east

shear zones which were likely to have been active at depths close to the frictional-viscous transition for dry plagioclase (Figure 10a), typically occuring at depths >20 km. At such depths, brittle seismic failure of the dry anorthosite host rock requires differential stresses in excess of hundreds of megapascals (Figure 10a). Hence, even when the stress drop is nearly complete (i.e., for $\Delta\tau/\tau$ in the range of 0.6–0.9, where $\Delta\tau$ is the earthquake stress drop and τ is the maximum shear stress on the seismogenic fault plane in the pre-earthquake stress field; Hardebeck & Okada, 2018), residual differential stresses during the postseismic period could be expected to be on the order of 100 MPa after a ~1-GPa coseismic stress drop. While long-term, steady-state viscous creep localized on the shear zones (including along the mylonitized pseudotachylytes) in Nusfjord may generally have taken place at more typical geological strain rates of 10^{-15}–10^{-13} s^{-1} (Fagereng & Biggs, 2019) under relatively low differential stresses during the interseismic period (i.e., blue curves in Figure 10a), transient higher differential stresses and strain rates, such as 10^{-9} s^{-1} derived in this study, can also be supported by localized viscous creep in the same material (orange curve in Figure 10a).

It has been suggested that transient high strain rate deformation and steady state low strain rate deformation may need to be accommodated in mechanically different materials, as proposed in relation to the postseismic behavior of the 1992 Landers earthquake (Ivins, 1996). However, given the high strength contrast between the pseudotachylyte shear zones and the surrounding, largely undeformed anorthosite, it is difficult to envisage long-term steady-state creep not being localized onto pseudotachylyte-bearing shear zones in Nusfjord. Pseudotachylyte-bearing shear zones were therefore able to support both low viscosity creep under transient high strain rates and higher viscosity deformation during steady state deformation, as indicated by localized overprint of lower stress foam-textured quartz. It may be that the quartz microstructures in the Nusfjord pseudotachylytes were predominantly preserved in the high stress state and recorded the lower stress stage only locally. The general preservation of high stress quartz microstructures is in accordance with experiments that suggest that quartz deformed at high stress and strain rate exhibits strong strain hardening (Hobbs, 1968), making it less likely to progressively change microstructure under subsequent reductions in stress or strain rate.

5.2. Timing of Transient High Stress and High Strain Rate Deformation in the Nusfjord Pseudotachylytes

Although the rheology of pseudotachylyte-bearing shear zones in the lower crust has been shown here to support short term episodes of elevated stress and strain rates during nonlinear viscous creep, there are two scenarios that could be proposed for when these transient conditions occurred. First, the high stress and strain rate transients could be part of the same seismic cycle that generated the pseudotachylytes, that is, occur almost immediately on crystallization of the pseudotachylyte on the cessation of coseismic slip. Alternatively, the pseudotachylytes could be somewhat or even very much older than a deformation event that generated high stresses and strain rates during localized viscous creep in the lower crust. Such an event could have potentially been the seismogenic reactivation of an overlying upper crustal fault zone, with a downward propagation of high stress in the lower crust (Ellis & Stöckhert, 2004). The timing of transient high strain rate and high differential stress creep cannot be easily constrained in the Nusfjord pseudotachylytes, but considering a cooling model and likely crystallization rates for these pseudotachylytes (Figure S5) suggests that solid-state viscous deformation could be accommodated within minutes to a couple of hours after the seismicity, which generated these veins (e.g., Ferrand et al., 2018). Given that pseudotachylytes in the Nusfjord shear zones were generated episodically within the period of long-term background viscous creep (Figure 1d), we propose that the observed transient high stress and high strain rate state (indicated by the fine-grained quartz) and subsequent lower stress overprint (indicated by the foam texture quartz) represent variations over a timescale of an earthquake cycles (Figure 10b). The high differential stress of 98 MPa is not envisaged to be the peak stress experienced during the seismic cycle, because the solid-state viscous deformation recorded in the fine-grained recrystallized quartz must take place only after crystallization of the pseudotachylyte melt has occurred and so the highest, immediately post-earthquake stress will have already decayed somewhat; however, significant stress perturbations in the lower crust are perhaps experienced for ~100 years or more (Ellis & Stöckhert, 2004). The strain rate of 10^{-9} s^{-1}, as recorded in these samples, is rare (or rarely preserved) in geological studies, with "typical" strain rates being 10^{-13}–10^{-15} s^{-1} (Fagereng & Biggs, 2019). On the geologically short timescales of earthquake cycles, the most likely driver of rapid aseismic strain rates is postseismic relaxation (Figure 10b).

5.3. Postseismic Relaxation as a Potential Driver of Transient High Stress and Strain Rate

Postseismic relaxation characterizes the ~100-year period immediately following seismic slip where rapidly relaxing high strain rates and stresses, and low but increasing crustal viscosities, are observed on and around the fault zone until some long-term interseismic steadystate is reached (Ingleby & Wright, 2017; Thatcher, 1983). Hence, if some of this postseismic relaxation is accommodated via viscous creep, any resultant deformation microstructure and recrystallization is expected to progressively evolve into a lower stress and lower strain rate deformation phase, potentially overprinting the transient high strain rate microstructures (Kidder et al., 2016; Trepmann & Stöckhert, 2003). In the Nusfjord psedutoachylytes, we see this expressed in the local development of foam-textured quartz. In order for the foam texture quartz (Figure 6) to feasibly represent an interseismic component of the seismic cycle (Figure 10b), the grain growth and annealing of quartz must also be able to produce a maximum grain size of ~30 μm from a minimum initial grain size of ~6.5 μm (Figure 6) within a timescale applicable to seismic cycles. Parameters for the static grain growth of quartz are available from Wightman et al. (2006), based on natural quartz samples, and from Fukuda et al. (2019), based on quartz grown under experimental conditions. Grain growth is modeled on the concept $d^n - {d_0}^n = kt$, where d is the grain size at time t, d_0 the initial grain size, k the rate constant, and n is the growth exponent (e.g., Fukuda et al., 2019). Using temperatures of 650°C–750°C and pressures of 0.7–0.75 GPa for steady-state deformation in the Nusfjord mylonitized pseudotachylytes (Menegon et al., 2017), and water fugacities calculated for these conditions (Tödheide, 1972), the minimum period necessary for transformation from the fine-grained recrystallized quartz to the foam texture ranges from 1–100 years, inversely proportional to temperature (Figure 10c). The grain growth parameters of Wightman et al., 2006 are somewhat pressure dependent, but those of Fukuda et al. (2019) are not, excepting the input of water fugacity. Although the more recent work of Fukuda et al. suggested that the temperature dependence of the Wightman et al. (2006) grain growth parameters might be overestimated, the timescales estimated by both methods are very similar under the Nusfjord deformation conditions. The 100-year timescale given by both estimates is completely compatible with the periodicity of seismic cycles.

In addition, the nonlinear mixed flow law that accounts for the combination of dislocation creep of quartz plus diffusion creep of the pseudotachylyte matrix is one of the accepted rheologies that can account for the observed rapid rates of postseismic strain rate decay (Ingleby & Wright, 2017). Such nonlinear creep may in fact be characteristic of pseudotachylytes where the conditions allow viscous deformation via dislocation creep of the coarser grained survivor clasts and surrounding damage zone in addition to the typical diffusion creep of the finer-grained pseudotachylyte matrix (Menegon et al., 2017; Passchier, 1982). Although the pseudotachylytes would remain able to viscously accommodate subsequent high stress and strain rate epsiodes for as long as they remained fine-grained at similar P-T conditions, it seems unlikely that they would not also accommodate the postseismic transients related to the coseismic event, which formed them in the first place. In conclusion, we suggest that the most likely origin of the observed stress and strain rate transients was postseismic relaxation and that the pseudotachylytes locally record the changing stresses and strain rates across a singe seismic cycle.

This study provides the first examination of recrystallized pseudotachylyte as an accommodator of rapid postseismic creep. However, glassy pseudotachylyte is also proposed to undergo viscous flow at temperatures found in the mid-crust and below, providing that the glass is wet (Proctor et al., 2017). Under these conditions, glassy pseudotachylyte experimentally shows low viscosities around 10^{12} Pa·s., several orders of magnitude lower than the viscosity predicted for recrystallized pseudotachylytes in Lofoten. However, the experimental samples of Proctor et al. (2017) differ widely from the Lofoten samples and many other exhumed natural pseudotachylytes, as they contain <1% crystals, no clasts, have pore water, and the mechanism of deformation is not intracrystalline plasticity and diffusion creep but flow of an amorphous matrix above the glass transition temperature (Proctor et al., 2017). While the conditions of deformation are different, the temperature control on where pseudotachylytes can accommodate postseismic creep is highly significant. At low temperatures equivalent to those in the upper crust, pseudotachylytes will be brittle and often as strong as, or stronger than, the surrounding rock, and will not localize later frictional failure after the coseismic event (Di Toro & Pennacchioni, 2005; Mitchell et al., 2016; Proctor et al., 2017). Thus, the proposed accommodation of postseismic deformation by viscous creep within pseudotachylytes is viable only in the mid-crust to lower crust where thermally activated creep mechanisms are dominant.

5.4. Lower Crustal Viscosity and Extent of Localization

Several geodetic observations of fault zone deformation at elevated strain rates are best explained by some contribution from creep on localized lower crustal shear zones (Kenner & Segall, 2003; Yamasaki et al., 2014), and both geological and numerical studies indicate that localization is generally expected at depth where the lower crust is relatively strong (Getsinger et al., 2013; Montési, 2004). This scenario is consistent with what we infer for Nusfjord east, where the transient high strain rate viscous creep was almost entirely localized on pseudotachylyte-bearing shear zones (Figures 2 and 3). The contribution to deformation from the wider coarse-grained anorthosite appears to have been insignificant, with little evidence from field observations that any deformation has occurred within it. Very little of the anorthosite can therefore have contributed to the deformation and bulk strain rate across the kilometer-scale shear zone network. Instead, viscous deformation must have continuously been highly localized onto the pseudotachylyte-bearing shear zones. Although the viscosity of the pseudotachylyte (~10^{16} Pa·s) during the high strain rate deformation is low relative to nondeforming or low strain rate lower crustal values, it is similar to some geodetic postseismic lower crustal and some localized geological estimates (Figure 9). The slight difference in magnitude between geodetic postseismic viscosities and the value derived here may be due to the difference in sampling scale between geodetic and microstructural studies and to the high level of localisation seen in the Nusfjord shear zones that may not be exactly comparable to some mature continental-scale faults sampled in geodetic studies. Generally, however, the similar viscosities suggest that high strain rate deformation, which is experienced during post-seismic relaxation, is in fact to some extent localized where it is accommodated within the lower crust, especially where the lower crust is known to be dry. This finding, alongside other recent work (Hussain et al., 2018; Ingleby & Wright, 2017; Yamasaki et al., 2014), highlights that postseismic studies of lower crustal viscosity—which are inherently undertaken in the vicinity of large fault zones—do not derive estimates of the viscosity of the normal lower crust. They instead likely reflect the heterogeneous viscosity across deep shear zones and the temporally varying viscosities induced by the initial earthquake. In light of this, we suggest that although our viscosity estimates are derived from narrow, highly localized shear zones, they nonetheless would be close to the viscosity that would be seen across the deep roots of the Nusfjord east shear zone network during the active high strain rate deformation by a geodetic survey, because of the extent of localization and lack of contribution to viscous creep from the host rock.

We highlight that, regardless of whether lower crustal pseudotachylytes are immediately overprinted by viscous creep after their solidification from coseismic melts or result from earlier deformation events but are reactivated by later viscous creep, they represent weak domains that could facilitate high strain rate deformation within the granulitic lower crust typical of thick continental interiors. If viscous creep immediately follows pseudotachylyte generation, as is shown to be possible from their rapid crystallization and cooling times, then additional effects such as the introduction of water into the dry and strong lower crust (Jamtveit et al., 2018) will amplify the local weakening effect.

6. Conclusions

Deformation recorded by pseudotachylyte-bearing mylonitic shear zones in Nusfjord east, Lofoten, indicates relatively high differential stress and rapid strain rates. The strain rate in particular, at ~10^{-9} s^{-1}, is several magnitudes faster than typical geological processes. Such elevated strain rates are interpreted to result from nonsteady-state flow associated with transient deformation of the lower crust, presumably during postseismic relaxation. Viscosities of deforming pseudotachylyte-bearing shear zones indicate similar values to transient lower crustal observations derived from geodetic studies on active fault zones, supporting the inference that transient high strain rate creep can be accommodated within lower crustal mylonitized pseudotachylytes. The strength contrast between the fine-grained pseudotachylyte and the surrounding anorthosite causes localization of the high strain rate and high stress deformation, and this is likely to be the case in many lower crustal shear zones hosted in dry, feldspar-rich lithologies.

Acknowledgments
This work was supported by the UK Natural Environment Research Council (grant NE/P001548/1 "The Geological Record of the Earthquake Cycle in the Lower Crust"). We thank Sandra Piazolo and Andrew Cross for their thorough and constructive reviews. The staff at the Plymouth University Electron Microscopy Centre are thanked for support during SEM analysis. We thank Tim Wright and Åke Fagereng for constructive discussion throughout the process of this study and for their friendly reviews of the manuscript, as well as Jean-Philippe Avouac and Christie Rowe for their constructive comments to an earlier version of the manuscript. According to the NERC data management policy, data are available at the British Geological Survey National Geoscience Data Centre (https://www.bgs.ac.uk/services/ngdc/accessions/index.html#item128606).

References

Austrheim, H. (2013). Fluid and deformation induced metamorphic processes around Moho beneath continent collision zones: Examples from the exposed root zone of the Caledonian mountain belt, W-Norway. *Tectonophysics*, *609*, 620–635. https://doi.org/https://doi.org/10.1016/j.tecto.2013.08.030

Austrheim, H., Erambert, M., & Boundy, T. M. (1996). Garnets recording deep crustal earthquakes. *Earth and Planetary Science Letters*, *139*(1–2), 223–238. https://doi.org/10.1016/0012-821X(95)00232-2

Behr, W. M., & Platt, J. P. (2014). Brittle faults are weak, yet the ductile middle crust is strong: Implications for lithospheric mechanics. *Geophysical Research Letters 41*, 2014GL061349. https://doi.org/10.1002/2014gl061349

Bürgmann, R., & Dresen, G. (2008). Rheology of the lower crust and upper mantle: Evidence from rock mechanics, geodesy, and field observations. *Annual Review of Earth and Planetary Sciences*, *36*, 531–567. https://doi.org/doi:10.1146/annurev.earth.36.031207.124326

Chopra, P. N. (1997). High-temperature transient creep in olivine rocks. *Tectonophysics*, *279*, 93–111. https://doi.org/10.1016/S0040-1951(97)00134-0

Corfu, F. (2004). U–Pb Age, setting and tectonic significance of the anorthosite–mangerite–charnockite–granite suite, Lofoten–Vesterålen, Norway. *Journal of Petrology*, *45*, 1799–1819.

Cross, A. J., Prior, D. J., Stipp, M., & Kidder, S. (2017). The recrystallized grain size piezometer for quartz: An EBSD-based calibration. *Geophysical Research Letters*, *44*, 6667–6674. https://doi.org/10.1002/2017GL073836

Cross, A. J., & Skemer, P. (2017). Ultramylonite generation via phase mixing in high strain experiments. *Journal of Geophysical Research: Solid Earth*, *122*, 1744–1759. https://doi.org/10.1002/2016JB013801

Di Toro, G., & Pennacchioni, G. (2005). Fault plane processes and mesoscopic structure of a strong-type seismogenic fault in tonalites (Adamello batholith, Southern Alps). *Tectonophysics*, *402*(1–4), 55–80. https://doi.org/https://doi.org/10.1016/j.tecto.2004.12.036

Dimanov, A., & Dresen, G. (2005). Rheology of synthetic anorthite-diopside aggregates: Implications for ductile shear zones. *Journal of Geophysical Research - Solid Earth*, *110*, 1–24. https://doi.org/10.1029/2004JB003431

Ellis, S., & Stöckhert, B. (2004). Elevated stresses and creep rates beneath the brittle-ductile transition caused by seismic faulting in the upper crust. *Journal of Geophysical Research - Solid Earth*, *109*(B05407), 1–10. https://doi.org/10.1029/2003JB002744

Fagereng, Å., & Biggs, J. (2019). New perspectives on 'geological strain rates' calculated from both naturally deformed and actively deforming rocks. *Journal of Structural Geology*, *125*,, 100–110. https://doi.org/10.1016/j.jsg.2018.10.004

Ferrand, T. P., Labrousse, L., Eloy, G., Fabbri, O., Hilairet, N., & Schubnel, A. (2018). Energy balance from a mantle pseudotachylyte, Balmuccia, Italy. *Journal of Geophysical Research: Solid Earth*, *123*, 3943–3967. https://doi.org/10.1002/2017JB014795

Fitz Gerald, J. D., Mancktelow, N. S., Pennacchioni, G., & Kunze, K. (2006). Ultrafine-grained quartz mylonites from high-grade shear zones: Evidence for strong dry middle to lower crust. *Geology*, *34*, 369–372. https://doi.org/10.1130/G22099.1

Floyd, M. A., Walters, R. J., Elliott, J. R., Funning, G. J., Svarc, J. L., Murray, J. R., et al. (2016). Spatial variations in fault friction related to lithology from rupture and afterslip of the 2014 South Napa, California, earthquake. *Geophysical Research Letters*, *43*, 6808–6816. https://doi.org/10.1002/2016GL069428

Fournier, H. W., Lee, J. K. W., Camacho, A., & Creaser, R. A. (2014). Retrogression of eclogite-facies shear zones by short-lived fluid infiltration during the Caledonian orogeny, Lofoten islands, Norway. *Geological Society, London, Special Publications*, *390*, 443–466. https://doi.org/10.1144/SP390.9

Freed, A. M., & Burgmann, R. (2004). Evidence of power-law flow in the Mojave desert mantle. *Nature*, *430*, 548–551.

Freed, A. M., Bürgmann, R., Calais, E., & Freymueller, J. (2006). Stress-dependent power-law flow in the upper mantle following the 2002 Denali, Alaska, earthquake. *Earth and Planetary Science Letters*, *252*, 481–489. https://doi.org/https://doi.org/10.1016/j.epsl.2006.10.011

Fukuda, J., Raimbourg, H., Shimizu, I., Neufeld, K., & Stünitz, H. (2019). Experimental grain growth of quartz aggregates under wet conditions and its application to deformation in nature. *Solid Earth*, *10*(3), 621–636. https://doi.org/10.5194/se-10-621-2019

Gardner, R. L., Piazolo, S., & Daczko, N. R. (2016). Shape of pinch and swell structures as a viscosity indicator: Application to lower crustal polyphase rocks. *Journal of Structural Geology*, *88*, 32–45. https://doi.org/https://doi.org/10.1016/j.jsg.2016.04.012

Getsinger, A. J., & Hirth, G. (2014). Amphibole fabric formation during diffusion creep and the rheology of shear zones. *Geology*, *42*, 535–538. https://doi.org/10.1130/G35327.1

Getsinger, A. J., Hirth, G., Stünitz, H., & Goergen, E. T. (2013). Influence of water on rheology and strain localization in the lower continental crust. *Geochemistry, Geophysics, Geosystems*, *14*, 2247–2264. https://doi.org/10.1002/ggge.20148

Hardebeck, J. L., & Okada, T. (2018). Temporal stress changes caused by earthquakes: A review. *Journal of Geophysical Research: Solid Earth*, *123*(2), 1350–1365. https://doi.org/10.1002/2017JB014617

Hawemann, F., Mancktelow, N. S., Wex, S., Camacho, A., & Pennacchioni, G. (2018). Pseudotachylyte as field evidence for lower-crustal earthquakes during the intracontinental Petermann Orogeny (Musgrave Block, Central Australia). *Solid Earth*, *9*, 629–648. https://doi.org/0.5194/se-9-629-2018

Hearn, E. H., Bürgmann, R., & Reilinger, R. E. (2002). Dynamics of Izmit earthquake postseismic deformation and loading of the Düzce earthquake hypocenter. *Bulletin of the Seismological Society of America*, *92*, 172–193. https://doi.org/10.1785/0120000832

Hearn, E. H., McClusky, S., Ergintav, S., & Reilinger, R. E. (2009). Izmit earthquake postseismic deformation and dynamics of the North Anatolian fault zone. *Journal of Geophysical Research - Solid Earth*, *114*. https://doi.org/10.1029/2008JB006026

Heilbronner, R., & Tullis, J. (2002). The effect of static annealing on microstructures and crystallographic preferred orientations of quartzites experimentally deformed in axial compression and shear. *Geological Society, London, Special Publications*, *200*(1), 191 LP–218. https://doi.org/10.1144/GSL.SP.2001.200.01.12

Herwegh, M., Linckens, J., Ebert, A., Berger, A., & Brodhag, S. H. (2011). The role of second phases for controlling microstructural evolution in polymineralic rocks: A review. *Journal of Structural Geology*, *33*(12), 1728–1750. https://doi.org/https://doi.org/10.1016/j.jsg.2011.08.011

Hetland, E. A., & Hager, B. H. (2003). Postseismic relaxation across the Central Nevada Seismic Belt. *Journal of Geophysical Research - Solid Earth*, *108*. https://doi.org/10.1029/2002JB002257

Hill, R. (1965). Theory of mechanical properties of fibre-strengthened materials—III. Self-consistent model. *Journal of the Mechanics and Physics of Solids*, *13*, 189–198. https://doi.org/10.1016/0022-5096(65)90008-6

Hirth, G., Teyssier, C., & Dunlap, J. W. (2001). An evaluation of quartzite flow laws based on comparisons between experimentally and naturally deformed rocks. *International Journal of Earth Sciences*, *90*, 77–87. https://doi.org/10.1007/s005310000152

Hirth, G., & Tullis, J. (1992). Dislocation creep regimes in quartz aggregates. *Journal of Structural Geology*, *14*(2), 145–159. https://doi.org/https://doi.org/10.1016/0191-8141(92)90053-Y

Hobbs, B. E. (1968). Recrystallization of single crystals of quartz. *Tectonophysics*, *6*, 353–401. https://doi.org/https://doi.org/10.1016/0040-1951(68)90056-5

Hussain, E., Wright, T. J., Walters, R. J., Bekaert, D. P. S., Lloyd, R., & Hooper, A. (2018). Constant strain accumulation rate between major earthquakes on the North Anatolian Fault. *Nature Communications*, *9*(1392). https://doi.org/10.1038/s41467-018-03739-2

Ingleby, T., & Wright, T. J. (2017). Omori-like decay of postseismic velocities following continental earthquakes. *Geophysical Research Letters*, *44*, 3119–3130. https://doi.org/10.1002/2017GL072865

Ivins, E. R. (1996). Transient creep of a composite lower crust: 2. A polymineralic basis for rapidly evolving postseismic deformation modes. *Journal of Geophysical Research - Solid Earth*, *101*, 28005–28028. https://doi.org/10.1029/96JB02846

Jamtveit, B., Ben-Zion, Y., Renard, F., & Austrheim, H. (2018). Earthquake-induced transformation of the lower crust. *Nature*, *556*, 487–491. https://doi.org/10.1038/s41586-018-0045-y

Jamtveit, B., Petley-Ragan, A., Incel, S., Dunkel, K. G., Aupart, C., Austrheim, H., et al. (2019). The effects of earthquakes and fluids on the metamorphism of the lower continental crust. *Journal of Geophysical Research: Solid Earth*, *0*(0). https://doi.org/10.1029/2018JB016461

Ji, S., Shao, T., Salisbury, M. H., Sun, S., Michibayashi, K., Zhao, W., et al. (2014). Plagioclase preferred orientation and induced seismic anisotropy in mafic igneous rocks. *Journal of Geophysical Research: Solid Earth*, *119*, 8064–8088. https://doi.org/10.1002/2014JB011352

Kenner, S. J., & Segall, P. (2003). Lower crustal structure in northern California: Implications from strain rate variations following the 1906 San Francisco earthquake. *Journal of Geophysical Research - Solid Earth*, *108*, ETG 5–1-ETG 5-17. https://doi.org/10.1029/2001JB000189

Kidder, S., Hirth, G., Avouac, J.-P., & Behr, W. (2016). The influence of stress history on the grain size and microstructure of experimentally deformed quartzite. *Journal of Structural Geology*, *83*, 194–206. https://doi.org/https://doi.org/10.1016/j.jsg.2015.12.004

Kilian, R., Heilbronner, R., & Stünitz, H. (2011). Quartz grain size reduction in a granitoid rock and the transition from dislocation to diffusion creep. *Journal of Structural Geology*, *33*, 1265–1284. https://doi.org/https://doi.org/10.1016/j.jsg.2011.05.004

Küster, M., & Stöckhert, B. (1999). High differential stress and sublithostatic pore fluid pressure in the ductile regime—Microstructural evidence for short-term post-seismic creep in the Sesia Zone, Western Alps. *Tectonophysics*, *303*(1–4), 263–277. https://doi.org/https://doi.org/10.1016/S0040-1951(98)00256-X

Markl, G., Frost, B. R., & Bucher, K. (1998). The origin of anorthosites and related rocks from the Lofoten Islands, Northern Norway: I. Field Relations and Estimation of Intrinsic Variables. *Journal of Petrology*, *39*, 1425–1452. https://doi.org/10.1093/petroj/39.8.1425

Matysiak, A. K., & Trepmann, C. A. (2012). Crystal–plastic deformation and recrystallization of peridotite controlled by the seismic cycle. *Tectonophysics*, *530–531*, 111–127. https://doi.org/https://doi.org/10.1016/j.tecto.2011.11.029

Mehl, L., & Hirth, G. (2008). Plagioclase preferred orientation in layered mylonites: Evaluation of flow laws for the lower crust. *Journal of Geophysical Research - Solid Earth*, *113*(B5). https://doi.org/10.1029/2007JB005075

Menegon, L., Nasipuri, P., Stünitz, H., Behrens, H., & Ravna, E. (2011). Dry and strong quartz during deformation of the lower crust in the presence of melt. *Journal of Geophysical Research - Solid Earth*, *116*, B10410. https://doi.org/10.1029/2011JB008371

Menegon, L., Pennacchioni, G., Malaspina, N., Harris, K., & Wood, E. (2017). Earthquakes as precursors of ductile shear zones in the dry and strong lower crust. *Geochemistry, Geophysics, Geosystems*, *18*, 4356–4374. https://doi.org/10.1002/2017GC007189

Mitchell, T. M., Toy, V., Di Toro, G., Renner, J., & Sibson, R. H. (2016). Fault welding by pseudotachylyte formation. *Geology*, *44*(12), 1059–1062. https://doi.org/10.1130/g38373.1

Montési, L. G. J. (2004). Postseismic deformation and the strength of ductile shear zones. *Earth, planets and space*, *56*, 1135–1142. https://doi.org/10.1186/BF03353332

Okudaira, T., Jeřábek, P., Stünitz, H., & Fusseis, F. (2015). High-temperature fracturing and subsequent grain-size-sensitive creep in lower crustal gabbros: Evidence for coseismic loading followed by creep during decaying stress in the lower crust? *Journal of Geophysical Research: Solid Earth*, *120*, 3119–3141. https://doi.org/10.1002/2014JB011708

Passchier, C. W. (1982). Pseudotachylyte and the development of ultramylonite bands in the Saint-Barthélemy Massif, French Pyrenees. *Journal of Structural Geology*, *4*, 69–79. https://doi.org/10.1016/0191-8141(82)90008-6

Paterson, M. S., & Olgaard, D. L. (2000). Rock deformation tests to large shear strains in torsion. *Journal of Structural Geology*, *22*(9), 1341–1358. https://doi.org/https://doi.org/10.1016/S0191-8141(00)00042-0

Petley-Ragan, A., Ben-Zion, Y., Austrheim, H., Ildefonse, B., Renard, F., & Jamtveit, B. (2019). Dynamic earthquake rupture in the lower crust. *Science Advances*, *5*(7), eaaw0913. https://doi.org/10.1126/sciadv.aaw0913

Piazolo, S., Bons, P. D., Jessell, M. W., Evans, L., & Passchier, C. W. (2002). Dominance of microstructural processes and their effect on microstructural development: Insights from numerical modelling of dynamic recrystallization. *Geological Society, London, Special Publications*, *200*(1), 149 LP–170. https://doi.org/10.1144/GSL.SP.2001.200.01.10

Pollitz, F. F., Wicks, C., & Thatcher, W. (2001). Mantle flow beneath a continental strike-slip fault: Postseismic deformation after the 1999 Hector Mine earthquake. *Science* (80-.), (293), 1814 LP–1818.

Price, N. A., Johnson, S. E., Gerbi, C. C., & West, D. P. (2012). Identifying deformed pseudotachylyte and its influence on the strength and evolution of a crustal shear zone at the base of the seismogenic zone. *Tectonophysics*, *518–521*, 63–83. https://doi.org/10.1016/j.tecto.2011.11.011

Proctor, B. P., Lockner, D. A., Lowenstern, J. B., & Beeler, N. M. (2017). Conversion of wet glass to melt at lower seismogenic zone conditions: Implications for pseudotachylyte creep. *Geophysical Research Letters*, *44*, 10,210–248,255. https://doi.org/10.1002/2017GL075344

Sibson, R. H. (1974). Frictional constraints on thrust, wrench and normal faults. *Nature*, *249*(5457), 542–544. https://doi.org/10.1038/249542a0

Sibson, R. H. (1980). Transient discontinuities in ductile shear zones. *Journal of Structural Geology*, *2*, 165–171. https://doi.org/10.1016/0191-8141(80)90047-4

Steltenpohl, M., Hames, W., Andresen, A., & Markl, G. (2003). New Caledonian eclogite province in Norway and potential Laurentian (Taconic) and Baltic links. *Geology*, *31*, 985–988. https://doi.org/10.1130/G19744.1

Steltenpohl, M. G., Hames, W. E., & Andresen, A. (2004). The Silurian to Permian history of a metamorphic core complex in Lofoten, northern Scandinavian Caledonides. *Tectonics*, *23*, TC4018. https://doi.org/10.1029/2003TC001522

Steltenpohl, M. G., Kassos, G., Andresen, A., Rehnström, E. F., & Hames, W. E. (2011). Eclogitization and exhumation of Caledonian continental basement in Lofoten, North Norway. *Geosphere*, *7*, 1–17. https://doi.org/10.1130/GES00573.1

Stipp, M., Stünitz, H., Heilbronner, R., & Schmid, S. M. (2002). The eastern Tonale fault zone: A 'natural laboratory' for crystal plastic deformation of quartz over a temperature range from 250 to 700 °C. *Journal of Structural Geology*, *24*, 1861–1884. https://doi.org/https://doi.org/10.1016/S0191-8141(02)00035-4

Thatcher, W. (1983). Nonlinear strain buildup and the earthquake cycle on the San Andreas fault. *Journal of Geophysical Research*, *88*(B7), 5893–5902. https://doi.org/10.1029/JB088iB07p05893

Tödheide, K. (1972). Water at high temperatures and pressures. In F. Franks (Ed.), *Water: A comprehensive treatise* (Vol. 1, chap. 13, pp. 463–514). New York: Springer.

Tokle, L., Hirth, G., & Behr, W. M. (2019). Flow laws and fabric transitions in wet quartzite. *Earth and Planetary Science Letters*, *505*, 152–161. https://doi.org/https://doi.org/10.1016/j.epsl.2018.10.017

Trepmann, C. A., & Stöckhert, B. (2003). Quartz microstructures developed during non-steady state plastic flow at rapidly decaying stress and strain rate. *Journal of Structural Geology*, *25*, 2035–2051. https://doi.org/https://doi.org/10.1016/S0191-8141(03)00073-7

Trepmann, C. A., Stöckhert, B., Dorner, D., Moghadam, R. H., Küster, M., & Röller, K. (2007). Simulating coseismic deformation of quartz in the middle crust and fabric evolution during postseismic stress relaxation—An experimental study. *Tectonophysics*, *442*, 83–104. https://doi.org/https://doi.org/10.1016/j.tecto.2007.05.005

Vergnolle, M., Pollitz, F., & Calais, E. (2003). Constraints on the viscosity of the continental crust and mantle from GPS measurements and postseismic deformation models in western Mongolia. *Journal of Geophysical Research - Solid Earth*, *108*. https://doi.org/10.1029/2002JB002374

Viegas, G., Menegon, L., & Archanjo, C. (2016). Brittle grain-size reduction of feldspar, phase mixing and strain localization in granitoids at mid-crustal conditions (Pernambuco shear zone, NE Brazil). *Solid Earth*, *7*, 375–396. https://doi.org/10.5194/se-7-375-2016

van der Werf, T., Chatzaras, V., Kriegsman, L. M., Kronenberg, A., Tikoff, B. R., & Drury, M. (2017). Constraints on the rheology of lower crust in a strike-slip plate boundary: Evidence from the San Quintin xenoliths, Baja California, Mexico. *Solid Earth.*, *2017*, 1–40. https://doi.org/10.5194/se-2017-45

Wex, S., Mancktelow, N. S., Camacho, A., & Pennacchioni, G. (2019). Interplay between seismic fracture and aseismic creep in the Woodroffe Thrust, central Australia—Inferences for the rheology of relatively dry continental mid-crustal levels. *Tectonophysics*, *758*, 55–72. https://doi.org/https://doi.org/10.1016/j.tecto.2018.10.024

White, J. C. (1996). Transient discontinuities revisited: Pseudotachylyte, plastic instability and the influence of low pore fluid pressure on deformation processes in the mid-crust. *Journal of Structural Geology*, *18*, 1471–1486. https://doi.org/10.1016/s0191-8141(96)00059-4

Wightman, R. H., Prior, D. J., & Little, T. A. (2006). Quartz veins deformed by diffusion creep-accommodated grain boundary sliding during a transient, high strain-rate event in the Southern Alps, New Zealand. *Journal of Structural Geology*, *28*(5), 902–918. https://doi.org/https://doi.org/10.1016/j.jsg.2006.02.008

Wright, S. I., Nowell, M. M., & Field, D. P. (2011). A review of strain analysis using electron backscatter diffraction. *Microscopy and Microanalysis*, *17*(3), 316–329. https://doi.org/10.1017/S1431927611000055

Yamasaki, T., Wright, T. J., & Houseman, G. A. (2014). Weak ductile shear zone beneath a major strike-slip fault: Inferences from earthquake cycle model constrained by geodetic observations of the western North Anatolian Fault Zone. *Journal of Geophysical Research: Solid Earth*, *119*, 3678–3699. https://doi.org/10.1002/2013JB010347

Zhao, B., Bürgmann, R., Wang, D., Tan, K., Du, R., & Zhang, R. (2017). Dominant controls of down-dip afterslip and viscous relaxation on the postseismic displacements following the Mw7.9 Gorkha, Nepal earthquake. *Journal of Geophysical Research: Solid Earth*, *122*, 8376–8401. https://doi.org/10.1002/2017JB014366

References From the Supporting Information

Carslaw, H. S., & Jaeger, J. C. (1959). *Conduction of Heat in Solids*. Oxford, UK: Oxford University Press.

Robie, R. A., & Waldbaum, D. R. (1968). Thermodynamic properties of minerals and related substances at 298.15°K (25.0°C) and one atmosphere (1.1013 bars) pressure and at higher temperatures. *USGS Geological Survey Bulletin*, 1259.

Sibson, R. H. (1975). Generation of pseudotachylyte by ancient seismic faulting. *Geophysical Journal of the Royal Astronomical Society*, *43*(3), 775. https://doi.org/10.1111/j.1365-246X.1975.tb06195.x

Spray, J. G. (2010). Frictional melting processes in planetary materials: From hypervelocity impact to earthquakes. *Annual Review of Earth and Planetary Sciences*, *38*, 221–254. https://doi.org/10.1146/annurev.earth.031208.100045